# Mitochondrial lipid droplet formation as a detoxification mechanism to sequester and degrade excessive urothelial membranes

Yi Liao[a,†,*], Daniel K. L. Tham[a,†], Feng-Xia Liang[a,†], Jennifer Chang[a], Yuan Wei[a], Putty-Reddy Sudhir[a], Joseph Sall[a], Sarah J. Ren[a], Javier U. Chicote[b], Lora L. Arnold[c], Chih-Chi Andrew Hu[d], Rok Romih[e], Leonardo R. Andrade[f], Michael J. Rindler[a], Samuel M. Cohen[c], Rob DeSalle[g], Antonio Garcia-España[b], Mingxiao Ding[h], Xue-Ru Wu[i,j,k], and Tung-Tien Sun[a,i,l,m,*]

[a]Department of Cell Biology, [i]Department of Urology, [k]Department of Pathology, [l]Department of Biochemistry and Molecular Pharmacology, and [m]Department of Dermatology, New York University School of Medicine, New York, NY10016; [b]Research Unit, Hospital Joan XXIII, Institut de Investigacio Sanitaria Pere Virgili (IISPV), Universitat Rovira i Virgili, Tarragona 43007, Spain; [c]Department of Pathology and Microbiology, University of Nebraska Medical Center, Omaha, NE 68198; [d]The Wistar Institute, University of Pennsylvania, Philadelphia, PA 19104; [e]Institute of Cell Biology, Faculty of Medicine, University of Ljubljana, SI-1000 Ljubljana, Slovenia; [f]Salk Institute, La Jolla, CA 92037; [g]Sackler Institute for Comparative Genomics, American Museum of Natural History, New York, NY 10024; [h]College of Life Sciences, Peking University, Dachengfang, Haidian, Beijing 100871, China; [j]Veterans Affairs Medical Center, New York, NY 10010

**ABSTRACT** **The apical surface of the terminally differentiated mammalian urothelial umbrella cell is mechanically stable and highly impermeable, in part due to its coverage by urothelial plaques consisting of 2D crystals of uroplakin particles. The mechanism for regulating the uroplakin/plaque level is unclear. We found that genetic ablation of the highly tissue-specific sorting nexin Snx31, which localizes to plaques lining the multivesicular bodies (MVBs) in urothelial umbrella cells, abolishes MVBs suggesting that Snx31 plays a role in stabilizing the MVB-associated plaques by allowing them to achieve a greater curvature. Strikingly, Snx31 ablation also induces a massive accumulation of uroplakin-containing mitochondria-derived lipid droplets (LDs), which mediate uroplakin degradation via autophagy/lipophagy, leading to the loss of apical and fusiform vesicle plaques. These results suggest that MVBs play an active role in suppressing the excessive/wasteful endocytic degradation of uroplakins. Failure of this suppression mechanism triggers the formation of mitochondrial LDs so that excessive uroplakin membranes can be sequestered and degraded. Because mitochondrial LD formation, which occurs at a low level in normal urothelium, can also be induced by disturbance in uroplakin polymerization due to individual uroplakin knockout and by arsenite, a bladder carcinogen, this pathway may represent an inducible, versatile urothelial detoxification mechanism.**

**Monitoring Editor**
Keith E. Mostov
University of California, San Francisco

Received: May 21, 2019
Revised: Sep 23, 2019
Accepted: Sep 27, 2019

This article was published online ahead of print in MBoC in Press (http://www.molbiolcell.org/cgi/doi/10.1091/mbc.E19-05-0284) on October 2, 2019.

[†]These authors contributed equally.

*Address correspondence to: Yi Liao (Yi.Liao@nyulangone.org); Tung-Tien Sun (sunt01@nyumc.org).

Abbreviations used: AP, autophagosome; As, arsenite; As3mt, arsenic (+3 oxidation state) methyltransferase; CCCP, carbonyl cyanide *m*-chlorophenyl hydrazine; DAPI, 4′, 6-diamidino-2-phenylindole; DV, discoidal vesicle; ER, endoplasmic reticulum; EST, expressed sequence tags; FV, fusiform vesicle; HRP, horseradish peroxidase; IB, immunoblotting; IEM, immunoelectron microscopy; ILD, incongruence length difference; ILV, intraluminal vesicle; IM, isolation membrane; IMS, mitochondrial intermembrane space; KO, knockout; LD, lipid droplet; Lys, lysosome; MMP, mitochondrial membrane potential; MT, mirrortree method; MVB, multivesicular body; NaAsIII, sodium arsenite; OM, mitochondrial outer membrane; OTO, O-osmium, T-thiocarbohydrazide, O-osmium; SEM, scanning electron microscopy; SH, Shimodaira-Hasegawa; SNX, sorting nexin; TEM, transmission electron microscopy; TGN, *trans*-Golgi network; UP, uroplakin; Wt, wild type.

© 2019 Liao, Tham, Liang, *et al*. This article is distributed by The American Society for Cell Biology under license from the author(s). Two months after publication it is available to the public under an Attribution–Noncommercial–Share Alike 3.0 Unported Creative Commons License (http://creativecommons.org/licenses/by-nc-sa/3.0).

"ASCB®," "The American Society for Cell Biology®," and "Molecular Biology of the Cell®" are registered trademarks of The American Society for Cell Biology.

## INTRODUCTION

The urinary bladder urothelium forms an exceptionally strong permeability barrier (Negrete *et al.*, 1996) separating the carcinogen-laden urine from the blood, and is a frequent site of tumor formation. In the United States, urothelial carcinoma of the bladder is the fourth- and twelfth-most common cancer in men and women, respectively (American Cancer Society, 2019). Owing to its multifocal and recurrent nature, urothelial carcinoma is the costliest cancer to manage on a per-patient basis (Lotan *et al.*, 2009). Moreover, the urothelial surface bears high-mannose receptors that allow the FimH adhesin of type 1–fimbriated *Escherichia coli* to bind, causing urinary tract infection, the most frequent bacterial infection type (Flores-Mireles *et al.*, 2015; Liu *et al.*, 2015).

The morphological hallmark of terminally differentiated urothelial umbrella cells is the accumulation of urothelial plaques that cover almost the entire apical surface and form numerous cytoplasmic plaque-delivering vesicles (Kachar *et al.*, 1999; Khandelwal *et al.*, 2009; Wu *et al.*, 2009). These plaques consist of 2D crystals of hexagonally packed 16-nm particles (Kachar *et al.*, 1999; Min *et al.*, 2006), which are formed by four major integral membrane proteins: the tetraspanins uroplakin Ia (UPIa) and UPIb (39% identical) and the single-pass UPII and UPIIIa (Wu *et al.*, 1990, 1994, 2009). Uroplakins first heterodimerize as UPIa/II and UPIb/IIIa pairs in the endoplasmic reticulum (ER; Tu *et al.*, 2002; Hu *et al.*, 2005), before being assembled into a heterotetramer (UPIa/II-Ib/IIIa) in the Golgi and *trans*-Golgi network (TGN), where they undergo chain-specific glycosylation and proteolytic processing (Hu *et al.*, 2005). Six such heterotetramers go on to form a 16-nm particle, many of which assemble into 2D crystals that are then delivered to the apical surface by the TGN-derived discoidal (DVs) and fusiform vesicles (FVs; Zhou *et al.*, 2012; Wankel *et al.*, 2016). UPIIIa is unique among the major uroplakins in possessing an ~50–amino acid–long cytoplasmic tail (Wu and Sun, 1993; Yu *et al.*, 1994), which plays a role in transmembrane signaling (Thumbikat *et al.*, 2009; Liao *et al.*, 2018). While previous studies of the UPII- and UPIIIa-knockout mice demonstrated the importance of uroplakins in maintaining the urothelial permeability barrier function and the flattening and enlargement of the umbrella cells (Hu *et al.*, 2000, 2002; Kong *et al.*, 2004), little is known about how uroplakin levels are regulated.

Earlier studies indicated that endocytosed apical uroplakin plaques are trafficked through the plaque-lined multivesicular bodies (MVBs) before their degradation in lysosomes (Amano *et al.*, 1991; Vieira *et al.*, 2014), but it remains unclear whether MVBs actually play an active role in regulating uroplakin degradation. We previously postulated that the MVB-localized sorting nexin 31 (Snx31), which is specifically expressed in the umbrella cells, disassembles uroplakins at the edges of the MVB-associated plaques (discussed more fully below), thus facilitating the invagination of uroplakin-containing membranes into intraluminal vesicles (ILVs) for lysosomal degradation (Vieira *et al.*, 2014).

Here, we show that Snx31 is a striking example of a tissue-specific MVB component that enables the processing of a tissue-specific cargo, uroplakin plaques in this case, for lysosomal degradation, and that MVBs play an active role in suppressing the endocytic degradation of uroplakins. We also show that the failure of MVB regulation triggers the massive accumulation of uroplakin-containing mitochondrial lipid droplets (LDs) as a means of degrading the excessive uroplakin membranes through an autophagy/lipophagy-type pathway in order to prevent them from forming insoluble cytotoxic aggregates (Tipping *et al.*, 2015; Nillegoda *et al.*, 2018). The fact that this mitochondrial LD pathway, which is rarely expressed in normal urothelium, is also induced by the depletion of uroplakins II or IIIa, and by arsenite, suggests that it functions as a versatile detoxification mechanism to sequester and eliminate excessive or imbalanced uroplakin membranes, and to protect the urothelium from arsenite, a commonly encountered bladder carcinogen.

## RESULTS

### Snx31 binds to uroplakin plaques of the MVBs

As mentioned, mouse urothelial umbrella cells accumulate copious amounts of uroplakin proteins associated with apical plaques and plaque-delivering FVs (Figure 1A). These cells also possess Snx31, which is restricted to the MVBs (Figure 1B and Supplemental Figure S1D; cf. Supplemental Figure S1E; Vieira *et al.*, 2014). Immunogold labeling showed that Snx31 was evenly distributed along the entire length of MVB-associated uroplakin plaques (Figure 1B), instead of being concentrated at the hinge region connecting two adjoining plaques as previously thought (Vieira *et al.*, 2014). Phylogenetic analyses showed that the *Snx31* gene coappeared with uroplakin genes in vertebrates, and codisappeared in bony fish (Figure 1C1). Evolutionary congruence test (Figure 1C2) showed that *UPIa* and *UPIb* genes coevolved with *UPII* and *IIIa* genes, respectively (Garcia-Espana *et al.*, 2006; Desalle *et al.*, 2014), consistent with their known protein pairing relationships (Wu *et al.*, 1995; Tu *et al.*, 2002; Hu *et al.*, 2005). This test also showed that *Snx31* coevolved with *UPIIIa* (Figure 1C2). Together with our earlier finding that anti-Snx31 antibody can pull down UPIIIa (Vieira *et al.*, 2014), these results revealed a coevolutionary relationship between Snx31 and the uroplakins, particularly UPIIIa.

### Snx31 knockout leads to the loss of uroplakin plaques, and the formation of uroplakin- and perilipin-positive LDs

To study the function of Snx31, we genetically ablated the mouse Snx31 gene, resulting in the loss of Snx31 at both the mRNA (Figure 1D1) and protein levels (Figure 1D2 and Supplemental Figure S1E; cf. Supplemental Figure S1D). As in the case of the *UPII* and *IIIa* knockouts that we had generated previously (Hu *et al.*, 2000, 2002; Kong *et al.*, 2004), the Snx31-deficient urothelium had a diminished uroplakin content, but to a lesser extent (a 50–60% reduction, compared with a 70–80% loss; Figure 1D2). Unlike normal umbrella cells, which are squamous and large (60–100 μm in diameter), with apical surfaces that are almost completely covered by uroplakin plaques (Figure 2A), superficial cells of the *Snx31*-KO urothelium were cuboidal/columnar and small (20–30 μm; Figures 1L, 2, B and E, and 3C; and see below), and had no discernible plaques (Figure 2B). This phenotype is similar to those of the *UPII*- (Figure 2C) and *UPIIIa*-KO urothelia (Figure 2D), and supports our suggestion that continued insertion of uroplakin plaques to the apical surface is crucial for umbrella cell enlargement (Hu *et al.*, 2002; Kong *et al.*, 2004). The *Snx31*-KO urothelium also accumulated numerous toluidine blue–positive structures resembling LDs (Figure 1, F1 and F2), which are absent in wild-type (Wt) urothelium (Figure 1E). Moreover, unlike normal superficial cells, which exhibited uniform cytoplasmic UP staining associated with uroplakin-delivering FVs (Figure 1G1), *Snx31*-KO superficial cells had reduced cytoplasmic UP staining, the majority of which became associated with the aforementioned LD-like structures (Figure 1, G2–G6). Double staining revealed precise colocalization of UPIa and UPII (of the Ia/II pair; Figure 1H), UPIb and IIIa (of the Ib/IIIa pair; unpublished data), and Ia/Ib (of the two pairs; unpublished data) in these LDs suggesting that the correct pairing relationships were maintained within the LDs. Time course studies revealed a progressive increase of these uroplakin-containing and

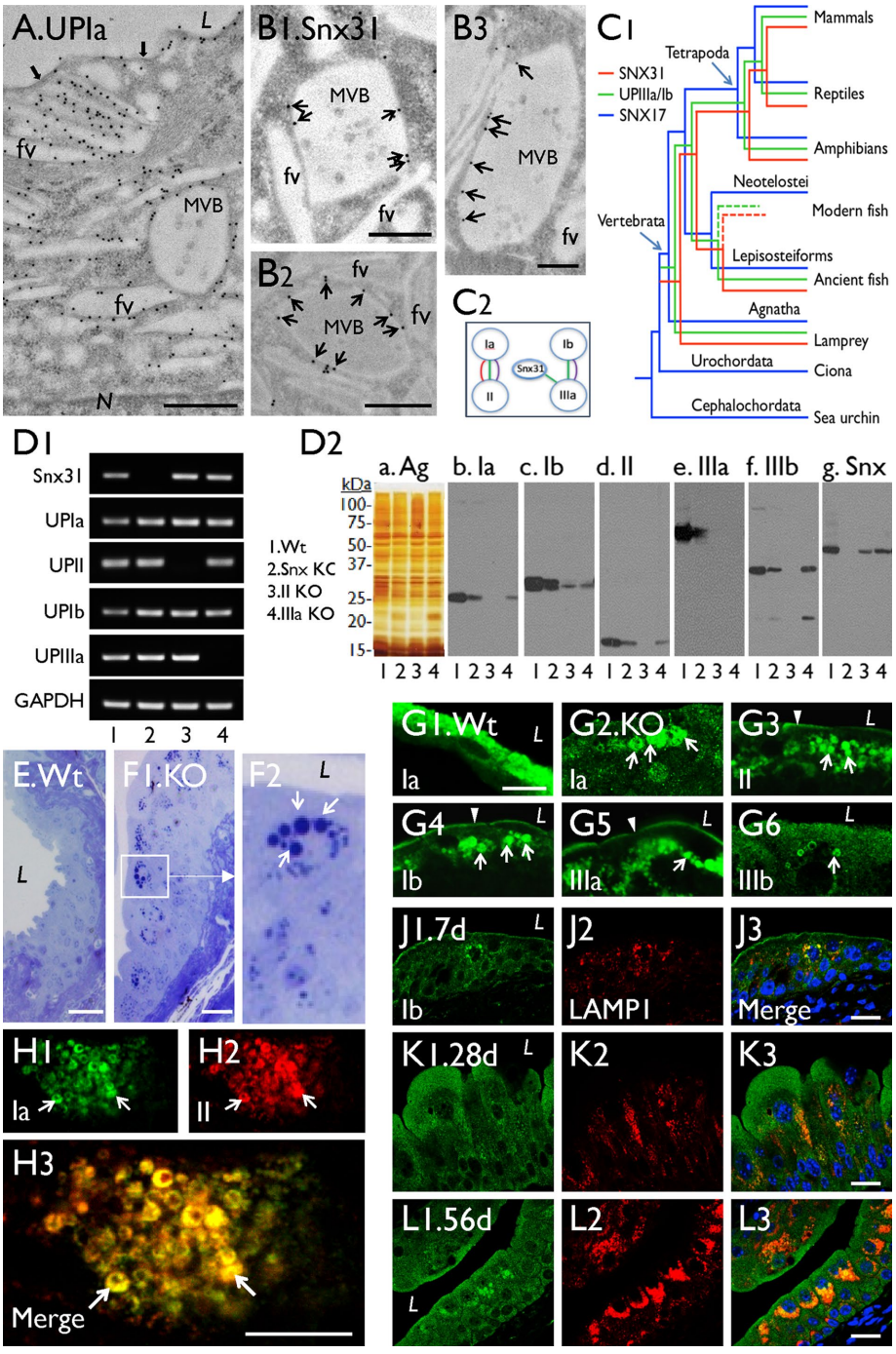


**FIGURE 1:** *Snx31* knockout leads to the loss of MVBs, reduced uroplakin content, and accumulation of lysosomes (related to Supplemental Figure 1). (A) Immunogold-EM localization of a mouse umbrella cell showing the association of uroplakins with apical plaques (black arrows), fusiform vesicles (FVs), and multivesicular body (MVB)-associated plaques. (B1–B3) Immunogold-EM localization of Snx31 (arrows) showing its association with the plaques of the MVB, but not with FVs. (C1) Coappearance of *uroplakin* and *Snx31* genes during vertebrate evolution, with *Snx17* gene as a "control" (see *Materials and Methods*). (C2) Evolutionary congruence analyses showing the sequence coevolution between genes encoding *uroplakins Ia/II*, *Ib/IIIa*, and *Snx31-UPIIIa* (the three colored connecting lines indicate coevolution as detected by different programs; see *Materials and Methods*). (D1) Detection of the *Snx31*, *UPIa*, *II*, *Ib*, *IIIa*, and *Gapdh* mRNA by RT-PCR in (1) wild type, (2) *Snx31*-KO, (3) *UPII*-KO, and (4) *UPIIIa*-KO. (D2) Immunoblot analyses of total membrane proteins (samples of lanes 1–4 corresponding to those of D1) after staining using (a) silver nitrate (Ag) or (b–g) monospecific antibodies as indicated. Five mice per line were sacrificed for protein collection. (E, F) Toluidine blue staining of Wt (E) and *Snx31*-KO (F1) urothelial sections showing the accumulation of cytoplasmic droplets (arrows) in the latter (F2 is a magnified view of the boxed area in F1). (G) Immunofluorescence staining of Wt (G1) and *Snx31*-KO urothelial sections (G2–G6) for uroplakins Ia, II, Ib, IIa, and IIIb as indicated; note in the KO urothelium the decrease in apical and (cytoplasmic) vesicle-associated uroplakins, which are now concentrated in droplet-like structures (arrows). (H) Double staining of UPIa and UPII in a *Snx31*-KO urothelial section showing their precise colocalization (arrows). (J–L) Double staining of UPIb (green) and lysosomal marker LAMP1 in urothelia of Snx31-KO mice that are 7, 28, and 56 d old, respectively. Note the progressively increasing accumulation of uroplakin-containing droplets surrounded by lysosomes. Scale bars = 0.5 µm in A and B; 10 µm in G and H; and 20 µm in E, F, J, K, and L.

LAMP1-associated droplets (Figure 1, J–L; from the 7-d-, 28-d-, and 56-d-old mice, respectively). These uroplakin-containing droplets were stained by probes for neutral lipids (Supplemental Figure S1F), phospholipids (Supplemental Figure S1G), and cholesterol (Supplemental Figure S1H), and many of them contained LD markers perilipin 1 and perilipin 2 (see later; Cohen, 2018), demonstrating their LD nature.

### The uroplakin-positive LDs originate from the mitochondria

Transmission EM showed that, unlike normal umbrella cells (Figures 1A and 3A), *Snx31*-KO urothelial superficial cells lacked MVBs and all other uroplakin-associated organelles, including apical plaques and the uroplakin-delivering FVs (Figure 3, B and C), and instead accumulated numerous LDs and lysosomes (Figure 3, B and C; and see later). The data also revealed a tremendous heterogeneity in the size, morphology, and number of LDs even among neighboring superficial cells (Figure 3B; unpublished data), most likely reflecting the significant size and protein composition changes as LDs mature (see Figure 11Q and Table 1 later in the paper). This heterogeneity unfortunately precludes meaningful quantification of the various LD types.

In general, urothelial LDs of young *Snx31*-KO mice (1 wk old) tended to be smaller than those of adult mice (2 mo old; Figure 1, J–L), suggesting that LDs enlarge over time before they are eventually digested by lysosomes (Figure 11Q and Table 1 later in the paper). We propose that the sequence of images shown in Figures 4, B–M and 5, A–H depicts various stages of LD maturation, which begins with small amorphous granules (0.2–0.3 µm) located in the intermembrane space of the mitochondrial cristae (Figure 4, B–K; early stage

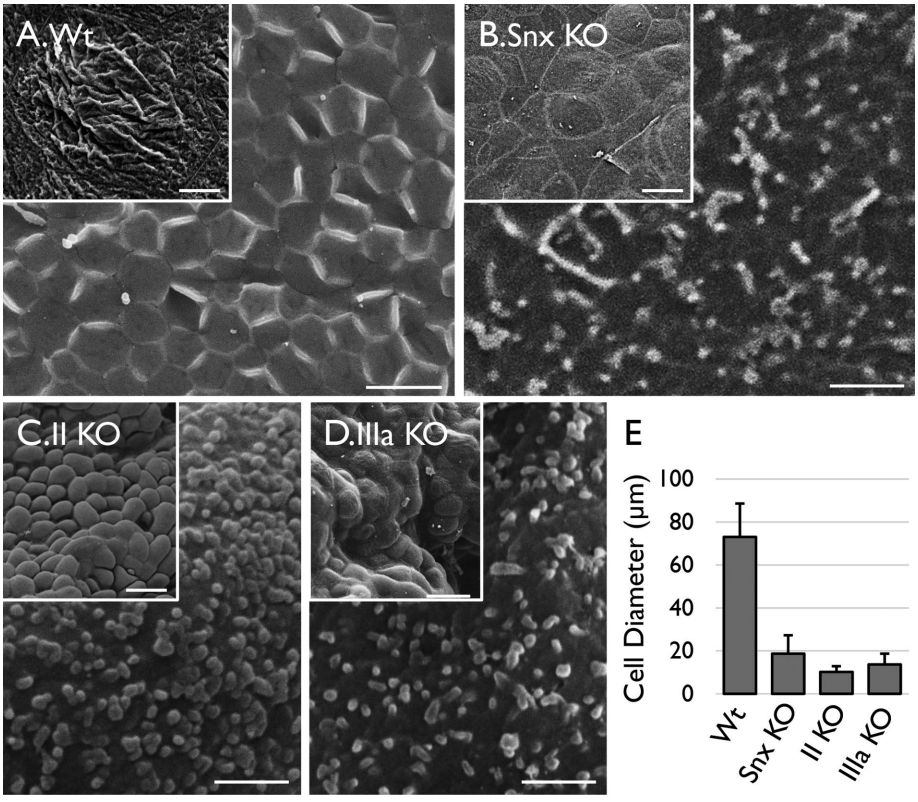


FIGURE 2: Superficial cells of *Snx31*-KO urothelium lack apical plaques and fail to enlarge. SEM images of (A) wild-type, (B) *Snx31*-KO, (C) UPII-KO, and (D) UPIIIa-KO bladder urothelial superficial cells showing that the *Snx31*-KO cells, like those of the UP-KOs, lack apical plaques (main images) and fail to enlarge (insets; see E for the measurement of the average cell diameters). SD based on the analysis of 20 cells. Scale bars = 1 μm in the main images and 20 μm in the insets.

I; *). Further enlargement of the LDs then leads to the reduction or complete disappearance of the mitochondrial cristae (Figure 4, L and M; stage II; **), and subsequently to partial (Figure 5, A and B) or complete cytoplasmic exposure of the LD (Figure 5, C and D; stage III; ***). Note in Figure 5C the striking size difference between a small intramitochondrial LD (0.2 μm diameter; *) on the left and a considerably larger "giant" LD (5 μm; ***) on the right (their different diameters equating to an ~($16 \times 10^3$)-fold volume difference). Also note in Figure 5, B and D, that while there was no space between the LD and the enclosing mitochondria (Figure 5B1 and star in 5B2), there was variable separation between the LD and the autophagosomal membranes (Figure 5D1 and star in 5D2). The tomography video in Figure 4N (Supplemental Video S1, A and B) and the serial block-face scanning electron microscopy (SEM) 3D model shown in Figure 4O (Supplemental Video SV2) clearly established the intramitochondrial location of the LDs. The LD-containing mitochondria and denuded LDs were enriched perinuclearly (Figure 3C and unpublished data) in proximity with the ER (arrowheads in Figures 4K and 5D1) and sometimes with autophagy-related isolation membranes (arrows in Figure 5, D–F). Some LDs appeared to be in the midst of undergoing fusion or fission with other LDs (Figure 5G), or entrapped within autophagic membranes, forming autophagosomes (APs; Figure 5J) or autolipophagosomes (ALs; Figure 5, K and L) in regions enriched in lysosomes (Figure 5, H, M, and N).

Immunogold labeling demonstrated that many Snx31-KO LDs, including the smaller intramitochondrial ones (Figure 6C) and giant denuded ones (Figure 6, B and D), and lysosomes (Figure 6E), contained uroplakins. In large LDs, some of the immunogold particles were seen to form linear streaks (Figure 6, D2–D5; see *Discussion*). The result also showed that the subapical spherical vesicles (~200 nm in diameter; Figure 3, C and F), also seen in UPII- and UPIIIa-KO urothelia (Hu *et al.*, 2000; Kong *et al.*, 2004), were uroplakin-negative (Figure 6B). These small subapical vesicles had no discernible uroplakin plaques, but may be involved in delivering residual uroplakins to the apical surface (Figure 10H later in the paper; Zhou *et al.*, 2012; Vieira *et al.*, 2014).

### The uroplakin-containing LDs are degraded via the autophagy-lysosomal pathway

The above data suggested that the progressive enlargement of intramitochondrial LDs may cause the mitochondria that house them to swell. To test this, we stained mitochondria in the whole-mount preparations of Wt and *Snx31*-KO mouse urothelia using Mito-ID Green. The results indicate that while most of the mitochondria of Wt urothelium were <1 μm in size (Figure 7A), more than 70% of the mitochondria of KO urothelium were in the range of 1–2 μm (Figure 7, B and C). We also stained the preparations using Mito-ID, which stains mitochondria with high membrane potential (MMP) red and those with low MMP green (the latter following treatment with carbonyl cyanide *m*-chlorophenyl hydrazine [CCCP], a mitochondrial oxidative phosphorylation uncoupler; Figure 7, D–J). These results indicate that the enlarged mitochondria of the KO urothelium had reduced MMP, consistent with the EM data showing mitochondrial damage (Figures 4 and 5).

To further establish the mitochondrial origin and the nature of the uroplakin-containing LDs, we examined their association with markers of several cellular processes. We found that, consistent with our EM data, antibody staining of the LDs was often heterogeneous, most likely reflecting the different stages of LD maturation (summarized in Table 1; Figure 11Q later in the paper). Many uroplakin-containing LDs were positive for AIF (Figure 7K) and COX4 (Figure 7O3), two mitochondrial markers residing in the intermembrane space (Wang *et al.*, 2012) and inner membrane (Ostrander *et al.*, 2001), respectively; PINK1 (Figure 7L), a mitophagy marker (Durcan and Fon, 2015); and perilipins 1 (PLIN1; Figure 7, M and O) and 2 (PLIN2; Figure 7N), two LD markers. The colocalization of uroplakins, mitochondrial, and lipid droplet markers in some of the LDs (Figure 7, K–O) established their mitochondrial origin.

To understand how uroplakins are delivered to mitochondrial LDs, we compared uroplakin trafficking in normal and *Snx31*-KO urothelia (Figure 8A). Consistent with our earlier data (Tu *et al.*, 2002; Hu *et al.*, 2005), Figure 8A (lanes 1–3 are from the Wt urothelium) illustrates that uroplakins traversing the ER/Golgi/TGN pathway underwent three types of secondary modifications that can be assessed by their sensitivities to endoglycosidases and by their protein size change. These include 1) the ER-mediated

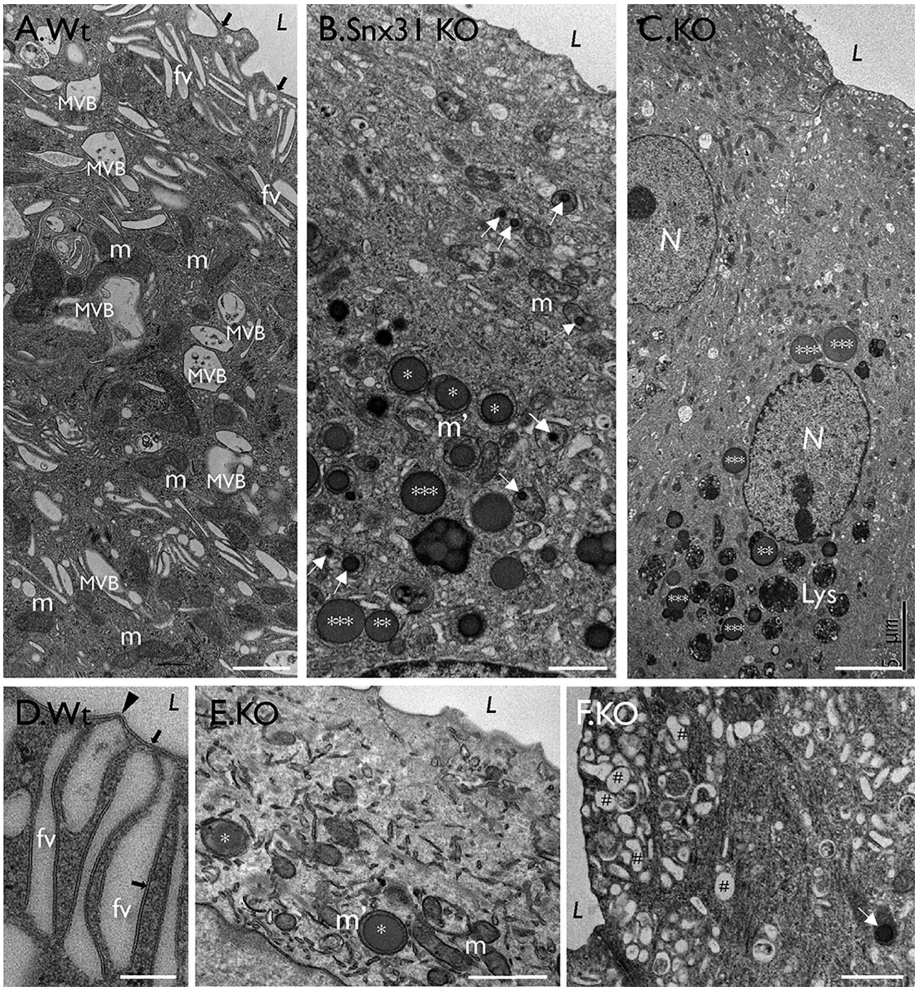


**FIGURE 3:** *Snx31*-KO urothelium loses fusiform vesicles and accumulates lipid droplets. TEM images showing (A) a typical normal bladder urothelial umbrella cell with normal mitochondria (m), apical uroplakin plaques (black arrows), fusiform vesicles (FVs); see (D) for a high-magnification view of FVs showing the plaques (arrow) and hinges (arrowhead). (B, C, E, and F) Superficial cells of the *Snx31*-KO bladder urothelium. Note the absence of typical plaques and FVs, and the accumulation of large LDs, some enclosed by a membranous structure (**) and some even larger, naked ones (***). Also note the accumulation of subapical small spherical vesicles (#). Scale bars = 0.2 μm in D; 1 μm in A, B, E, and F.

formation of Endo H–sensitive high-mannose glycans (e.g., UPIa; Figure 8Ac, lanes 1–3); 2) the Golgi-mediated complex glycan formation (which confers Endo H resistance and PNGase F sensitivity; e.g., UPIb and UPIIIa; Figure 8, Ae and Af, lanes 1–3); and 3) the TGN-furin–mediated proteolytic processing of the 32-kDa pro-UPII to yield the 15-kDa mature UPII (Figure 8Ad, lane 1; see model in Figure 11P later in the paper). Similar results were obtained with uroplakins of the *Snx31*-KO urothelium (lanes 4–6 in Figure 8A), except that two of the three UPIIIa-glycans remained Endo H sensitive, indicating incomplete Golgi-mediated complex glycan formation (Figure 8Af, lanes 4–6). These data established that uroplakins must also traverse through the ER/Golgi/TGN even in the Snx31-deficient urothelium (see model in Figure 11Q later in the paper). This conclusion is further supported by our finding that the uroplakin-positive LDs from the Snx31-deficient urothelium colocalized with the ER markers Sec23a (Figure 8B; Fromme *et al.*, 2008; Lord *et al.*, 2013), calnexin (Figure 8, C and D), and TGN marker TGN38 (Figure 8F), although not with GM130 (Figure 8E; a Golgi marker).

To study how the mitochondria-originated, uroplakin-containing LDs are eventually degraded, we double-stained mouse urothelia using antibodies to uroplakins and several markers for the degradative pathways. Our results showed that some of the uroplakin-positive LDs colocalized with LC3 (Figure 9, A–C), an autophagy marker (Soreng *et al.*, 2018) that showed significant activation in the *Snx31*-KO urothelium (Figure 9D), and LAMP1 (Figure 9E2), a late endosome/lysosome marker (Eskelinen, 2006). However, these uroplakin-containing LDs did not colocalize with EEA1 (Supplemental Figure S1J), an early endosome marker (Mu *et al.*, 1995). Finally, 20–30% of the superficial cells appeared to be undergoing apoptosis, based on the fact that they were caspase 3 (Figure 9E3) and TUNEL (Figure 9F4) positive, and contained nuclear fragments (Figure 9E4; Kyrylkova *et al.*, 2012; Larsen and Sorensen, 2017).

### Mitochondrial LDs are also induced in uroplakin KOs and after arsenite treatment

To see whether the mitochondrial LD pathway is unique to the *Snx31*-KO urothelium, we closely reexamined the *UPII*- or *UPIIIa*-KO urothelium, which as we reported earlier has imbalanced and misassembled uroplakins (Hu *et al.*, 2000; Kong *et al.*, 2004), to see whether they develop mitochondrial LDs. Interestingly, similar mitochondrial LDs were seen in the superficial cells of both *UPIIIa*-KO (Figure 10, D–G) and *UPII*-KO (Figure 10J showing immunogold labeling of uroplakins in the intramitochondrial LDs). The apical surface of *UPIIIa*-KO urothelium was distinct in that it had small patches of abnormally shaped 2D crystals (Figure 10H) probably corresponding to the remaining UPIa/II-UPIb/IIIb tetramer. (Note in the UPIIIa-knockout urothelium the formation of a unique uroplakin tetraheteromer UPIa/II-UPIb/IIIb in which UPIIIa is replaced by its minor isoform UPIIIb; Deng *et al.*, 2002; Desalle *et al.*, 2014.) This may explain why in the *UPIIIa*-KO the remaining UPs formed distinct perinuclear mitochondrial aggregates (Figure 10, C1–C5) visible by immunofluorescence. Similar to the *Snx31*-KO, the mitochondrial LDs from the *UPIIIa*-KO were positive for markers for LD (perilipin 2; Figure 10L), mitochondria (AIF; Figure 10M), mitophagy (PINK1; Figure 10N), and ER stress (BiP; Figure 10O), but not for the early endosome marker EEA1 (unpublished data). In contrast to the *Snx31*-KO, the uroplakin-positive LDs of the *UPIIIa*-KO were only minimally associated with LC3 (Figure 10M3) and LAMP1 (Figure 10P) probably because the smaller amounts of imbalanced uroplakins in these mutants placed a lighter demand on lysosomal degradation.

Intramitochondrial spherical inclusion bodies have been observed in the urothelia of the arsenite (As)-treated Wt and methyltransferase knockout (*Asmt3*-KO) mice (Suzuki *et al.*, 2008), a well-established model system for studying arsenite toxicity (Dodmane *et al.*, 2014). Feeding such mice with sodium arsenite-containing

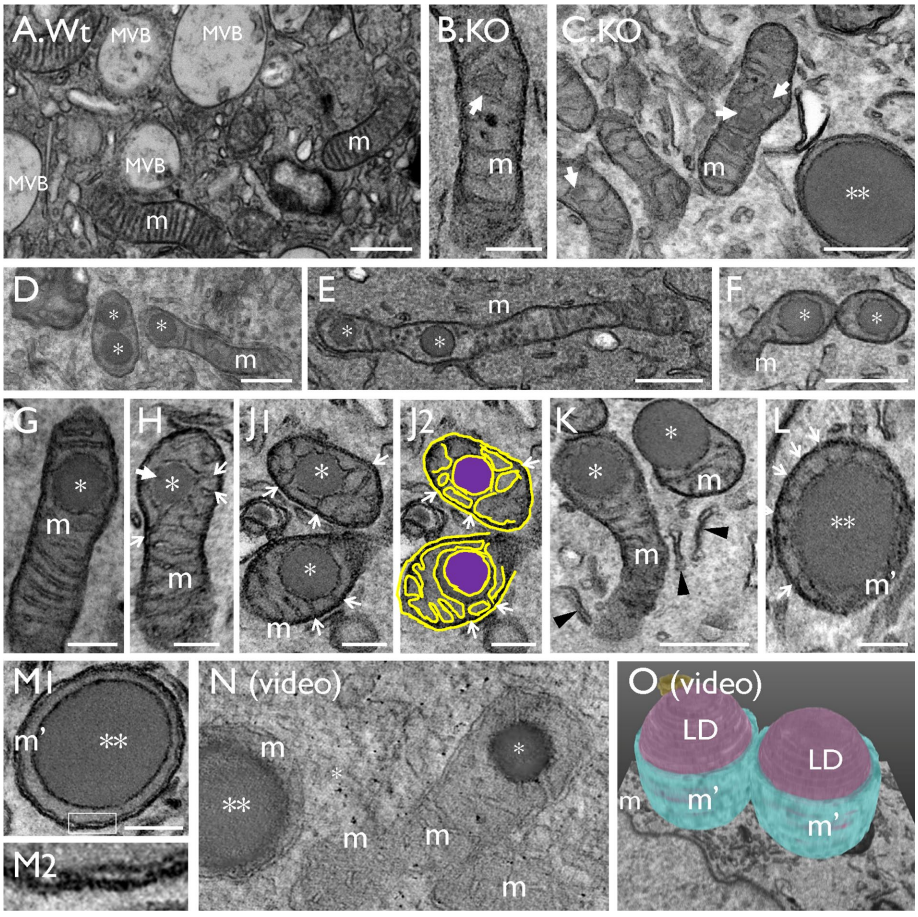


FIGURE 4: Lipid droplets originate from the mitochondria (related to Supplemental Videos 1A and 2). TEM images showing (A) a normal mouse bladder urothelial umbrella cell with multivesicular bodies (MVBs) and mitochondria (m). (B, C) Initiation of LD formation (arrow) in mitochondrion (m). (D–K) Small LDs (*; "stage I" in morphologically recognizable mitochondria) in the intermembrane space surrounded by the inner membrane of the mitochondrial cristae (arrows; J2 is a tracing of the image in J1); arrows mark the cristae connected to the LDs. A larger, "stage II" LD (**) surrounded by a small amount of mitochondria (L) with strings of residual cristae (arrows), or (M) without any more recognizable cristae structures; M2 is a high-magnification view of the boxed area in M1 showing the presence of a double-layered mitochondrial membrane (arrows). (N) A tomographic video (see Supplemental Video SV1A) and (O) a serial block-face SEM 3D model (see Supplemental Video SV2) showing that the LDs are indeed intramitochondrial. Scale bars = 0.2 μm in B, G, H, J, L, and M; 0.5 μm in A, C, D, E, F, and K.

drinking water induced the formation of spherical mitochondrial inclusion bodies in their urothelium (Suzuki *et al.*, 2008; Dodmane *et al.*, 2014). Transmission electron microscope (TEM) images showed that these inclusion bodies were morphologically similar to those of the *Snx31*-KO and *UP*-KO (Figure 11, A–C and D–G). Immunofluorescence staining indicated that the urothelium of the As-treated mouse was distinct from the Snx31-KO urothelium in that 1) it had normal uroplakin staining (Figure 11H) consistent with TEM data showing normal apical plaques (Figure 11, D and E, arrows) and FVs, indicating that in this case the mitochondrial LDs were not involved in uroplakin degradation; 2) most of the LDs were still intramitochondrial (Figure 11, D–F) with few reaching the denuded stage (Figure 11G shows a rare partially denuded LD); and 3) there was very little indication of autophagy-mediated lysosomal degradation. Additional data showed that, while the urothelium of As-treated mice also had increased staining of mitochondrial (Figure 11J) and ER stress markers (Figure 11, K and L), it had weak LAMP1 staining (Figure 7, M and N) suggesting a low level of lysosomal involvement. Another distinguishing feature of the bladder of As-treated mice is that there were numerous TUNEL-positive urothelial as well as mesenchymal cells indicating a broader involvement of apoptosis than in the *Snx31*-KO and *UP*-KO where it was limited to the urothelium itself (Figure 11O2 vs. 9F4).

Finally, we observed that normal urothelial cells of the Wt mice contained a few small intramitochondrial LDs (Figure 10K), suggesting that LD formation is part of a normal detoxification process that operates at a low level in normal urothelium but is activated when there is a need to remove excessive and/or misassembled membrane proteins or toxins, as discussed below.

## DISCUSSION

### Models illustrating Snx31 function and mitochondrial LD–mediated lysosomal degradation of imbalanced/misassembled uroplakin membranes

We present here two models that can account for all the available data regarding the trafficking of uroplakins in normal urothelial umbrella cells (Figure 11P) and in the superficial cells of *Snx31*-KO, *UPII- and UPIIIa*-KO, and As-treated mice (Figure 11Q). In normal umbrella cells, uroplakin proteins pass through the ER/Golgi/TGN export pathway (Figure 8A), giving rise to DVs that mature into FVs, which deliver uroplakin plaques to the apical surface (Hu *et al.*, 2005; Zhou *et al.*, 2012; Wankel *et al.*, 2016). These plaques are subsequently endocytosed to undergo MVB-mediated lysosomal degradation (Figure 11P). Our finding that the loss of MVBs caused by *Snx31*-KO leads to the collapse of uroplakin proteostasis (Figures 1D2, and 3, B and C) revealed that MVBs play a role to suppress the endocytic degradation of uroplakins (Figure 11P). The model in Figure 11Q depicts what takes place in *Snx31*-KO superficial cells. In addition to losing all uroplakin-associated structures (Figures 2B and 3, B and C), the mitochondria of these cells accumulate LDs (Figures 4, D–M, 5, A–F, and 7, A, B, and M–O) that continuously enlarge over time, resulting in the mitochondrial rupture and the formation of giant LDs that are partially or completely exposed to the cytoplasm (Figure 5, A–G). The intramitochondrial and exposed LDs have a similar density of uroplakin (as visualized using immunogold particles; Figure 6, C vs. D), suggesting that LDs continue to accumulate uroplakins as they expand in size. In contrast, aresenite-induced mitochondrial LDs undergo only limited expansion (Figure 11D), with very few LDs becoming denuded (vertical bar marked As in Figure 11Q indicating the approximate "blockage" point). Arsenite also triggers only limited autophagy-mediated lysosomal degradation (Figure 11, M and N). It is worth noting that we chose to use mouse bladder tissues in this study as cultured urothelial cells undergo an alternative pathway of differentiation that does not result in the formation of umbrella cells (Sun, 2006).

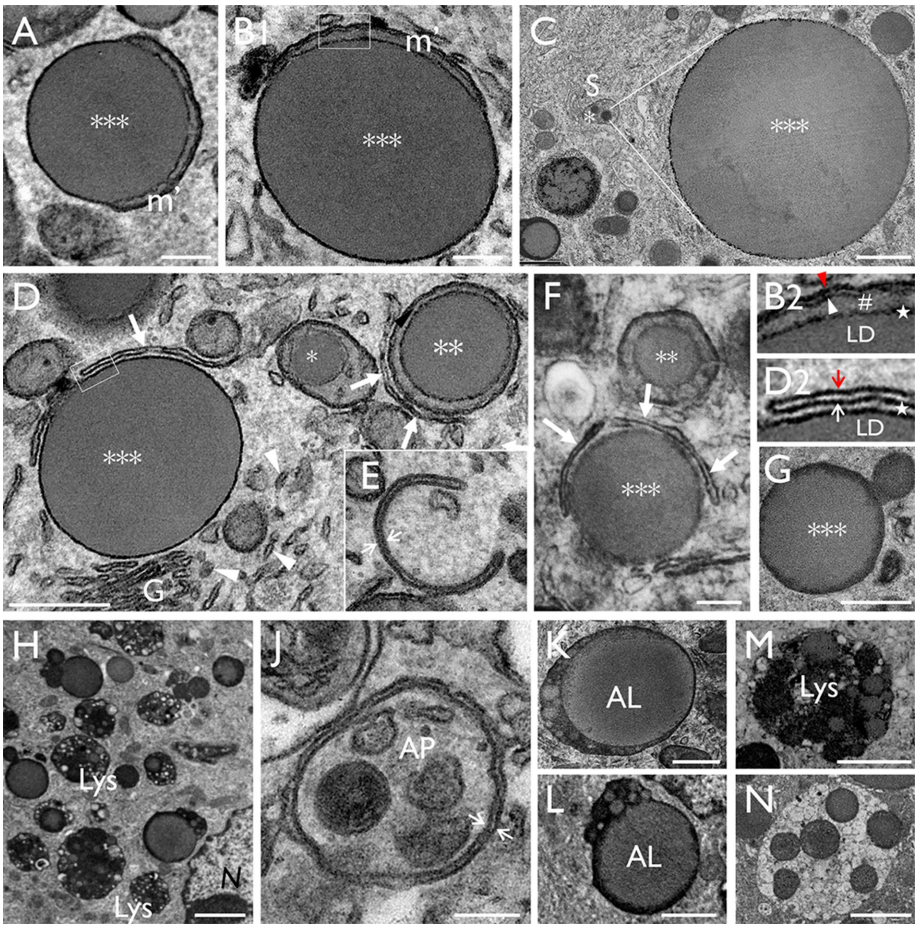


FIGURE 5: Urothelial LDs are degraded via the autophagy-lysosome pathway. (A–C) The continued expansion of mitochondrial LDs led to partially denuded (A, B) or completely denuded (C) LDs (***; stage III). Note in C the relative size difference between a newly formed stage I (*) intramitochondrial LD (0.2–0.4 µm) and a giant stage III denuded LD (4–5 µm). (D) Close proximity between the mitochondrial LDs with ER (arrowheads), Golgi (G), and autophagosomal membranes (arrows). B2 and D2 show the higher-magnification views of the boxed areas in B and D, respectively; the star in B2 highlights the intimate association between LD and its surrounding mitochondria, and that in D2 highlights the variable space between LD and the autophagosomal membrane. The red and white arrowhead/arrow in B2 and D2 denote the outer and inner membranes of the mitochondria and isolation membranes, respectively. (E) An autophagosomal "isolation membrane" (white arrows). (F) A large LD (***) partially surrounded by isolation membranes. (G) Possible fusion/fission of LDs. (H) The close proximity of large LDs with lysosomes. (J) A presumed autophagosome (AP) enclosing LD-containing mitochondria. (K, L) Two large LDs fusing with lysosomes forming autophagosomes/autolipophagosomes (ALs). (M, N) A lysosome and a possible secondary lysosome, respectively. Scale bars = 0.2 µm in A, B, E, F, and J; 0.5 µm in D1 and K; 1 µm in C, E, G, L, and M; and 2 µm in H and N.

### Snx31 may represent a mechanism allowing MVB-associated uroplakin plaques to adopt a greater degree of curvature

MVBs are present in most cell types and play key roles in the endocytic digestion of plasma membrane components and the generation of exosomes (Piper and Katzmann, 2007; Hanson and Cashikar, 2012). MVBs of all cell types share certain common proteins such as the ESCRT machinery that facilitates the invagination of cargo membrane proteins into the MVB lumen to form ILVs for lysosomal degradation (Piper and Katzmann, 2007; Hanson and Cashikar, 2012). Snx31 stands out as an umbrella cell–specific MVB protein that enables the MVBs to process a cargo unique to this cell type, that is, the rigid-looking 2D crystalline uroplakin plaques, which otherwise pose a particular challenge to the formation and function of MVBs.

We show here that Snx31, a bladder-specific phosphatidylinositol 3-phosphate–binding sorting nexin (Vieira *et al.*, 2014), plays a crucial role in regulating uroplakin levels in terminally differentiated urothelial umbrella cells, based on the following findings: 1) Snx31 is associated with the entire length of the plaques (Figure 1, B1–B3; cf. Vieira *et al.*, 2014); 2) Snx31, a cytoplasmic protein, coimmunoprecipitates with UPIIIa, the only uroplakin possessing a long cytoplasmic tail (Vieira *et al.*, 2014); and 3) *Snx31*-KO leads to the loss of MVBs and, concurrently, a large-scale lysosomal degradation of uroplakins (Figures 1D2 and 6E). Because the binding of FimH, the lectin of the uropathogenic *E. coli*, to its receptor UPIa (Zhou *et al.*, 2001) can induce global conformational changes of the plaque (Wang *et al.*, 2009), we hypothesize that the selective binding of Snx31 to the cytoplasmic tail of the plaque-associated UPIIIa can induce similar conformational changes in these plaques (Figure 11P, bottom inset). This may increase the flexibility of the otherwise rigid plaques, enabling them to adopt a greater curvature required for their 1) incorporation into the MVB (300–600 nm diameter) and 2) subsequent invagination into the lumen of the MVB to form the even smaller ILVs (20–40 nm diameter) suitable for lysosomal degradation (Figure 11P, bottom inset). Such functional interactions between Snx31 and UPIIIa may explain their coevolution (Figure 1, C1 and C2), and why the loss of Snx31 leads to the failure of MVB assembly (Figure 3, B and C).

### Mitochondrial LD formation is a versatile detoxification mechanism

An important outcome of this study is the observation that knocking out Snx31 induces the formation of intramitochondrial LDs (Figures 1 and 3–6). Although mitochondrial inclusion bodies (Schapira, 2012; Vincent *et al.*, 2016) and cytoplasmic LDs (Pol *et al.*, 2014; Wilfling *et al.*, 2014) are both common occurrences in diseases and other conditions causing cellular stress, the formation of intramitochondrial spherical inclusion bodies is rare and has been described only in frog oocytes (Massover, 1971) and urothelia of As-treated mouse (Suzuki *et al.*, 2008). However, these earlier findings were based on a limited number of low-magnification TEM images. In this study, we provide the first evidence that the intramitochondrial spherical inclusion bodies of mouse urothelia are in fact LDs (Figure 7, M–O, and Supplemental Figure S1, F–H).

Our data established that intramitochondrial LD formation is not limited to the urothelia of *Snx31*-KO animals, as it also occurs in the urothelia of uroplakin KOs (Figure 10) and As-treated mice (Figure 11), and even as a rare event in normal urothelium (Figure 10K). These results indicate that the mitochondrial LD pathway operates at a low baseline level in normal urothelium, but is up-regulated

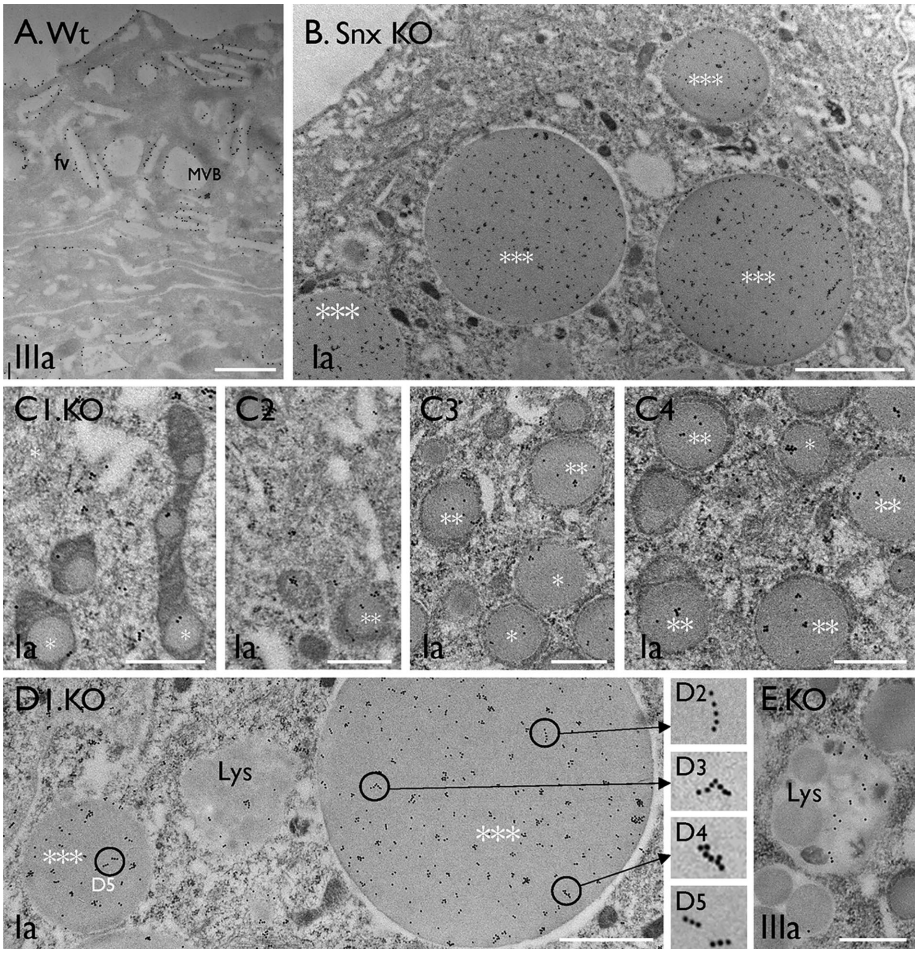


**FIGURE 6:** Uroplakins are present throughout mitochondria-originated LDs. Immunogold-EM localization of uroplakins (UPs) using monospecific antibodies in urothelial superficial cells of (A) wild-type and (B–E) *Snx31*-KO mice. Note in B the subapical small vesicles are UP-free; and in C and D the presence of uroplakins in all three stages of LDs (stages I–III). Note in D2–D5 the uroplakin-associated immunogold particles in a large LD often form linear arrays. (E) A secondary lysosome containing residual uroplakins. Scale bars = 0.5 μm in C and E; 1 μm in A and D; and 2 μm in B.

when there is a need to remove excessive/misassembled uroplakin membranes and lipids, or when the urothelium is challenged with arsenite. Although it has been suggested that As may be sequestered in these mitochondrial LDs (Suzuki *et al.*, 2008; Dodmane *et al.*, 2014), additional studies are needed to test this possibility.

Our finding that As treatment led to only the early steps of LD formation (Figure 11, D–G) and does not cause uroplakin dysregulation (Figure 11, E and H) is important, as it establishes that LD formation and membrane incorporation/degradation represent two separate processes (Figure 11Q). With regard to LD formation, the fact that early LDs are located in the intermembrane space (IMS; Figure 4, G–J) indicates that the process begins with fatty acid and phospholipid accumulation in the IMS (although the precise mechanisms by which this occurs is currently unknown). The intramitochondrial and denuded LDs are then incorporated into autophagosomes and autolipophagosomes (lipophagy; Wang, 2016), respectively, resulting in lysosomal degradation.

Many proteins that play important roles in the pathogenesis of neurodegenerative diseases enter into the mitochondria via the TOM import machinery (Lin and Beal, 2006; Hansson Petersen *et al.*, 2008; Tipping *et al.*, 2015). For example, it has been shown that the amyloid β-peptide (Hansson Petersen *et al.*, 2008) and aggregates of cytosolic proteins are imported into the mitochondria via the mitochondrial import machinery (Ruan *et al.*, 2017). The mitochondrial LD pathway is quite different. Our EM localization data indicate that uroplakins are incorporated uniformly in both small intramitochondrial LDs (Figure 6C) and giant cytoplasmically exposed LDs (Figure 6D), suggesting a continued uroplakin/lipid uptake during LD expansion starting when the LD is still contained within the mitochondria and continuing after the LD has become exposed. Because the expansion of LDs causes the damage/loss of mitochondrial cristae (Figures 4, G–M, and 7, A–J) and because protein aggregates can disrupt membranes (Lashuel, 2005; Glabe, 2006), it is possible that the uroplakin/lipid complex is initially delivered to intramitochondrial LDs through the damaged mitochondrial membranes (Figures 4, G–M, and 7, A–J), and then directly to the LDs once they emerge (Figure 5, A–C), thus bypassing the normal mitochondrial protein importing mechanisms (Hansson Petersen *et al.*, 2008; Wiedemann and Pfanner, 2017; Liu *et al.*, 2018). Another interesting feature of the mitochondrial LD pathway is that uroplakins can be delivered even to the center of the LD core (Figure 6, B and D1), rather than being limited to the LD surface as current dogma might suggest (Cohen, 2018; Olzmann and Carvalho, 2019). This observation is reminiscent of the earlier data by Robenek *et al.* (2011), who showed by freeze-fracture replica immunogold labeling that LDs form multilayered, onion-like structures with proteins detectable throughout the core, possibly in association with these lipid layers. This may explain why uroplakins can be found in the center of the LDs, and why uroplakin-associated immunogold particles were sometimes seen to form linear arrays (Figure 6, D1–D5), which may represent sections of uroplakin-containing membranes.

Regarding the mechanism by which the uroplakins are delivered to the LDs, our data indicate that uroplakins of the Snx31-KO urothelium must have transited through the usual ER/Golgi/TGN route, based on uroplakins' endoglycosidase and protease sensitivities (Figure 8A). It is interesting that, in the Snx31-KO urothelium, the LD-associated uroplakins colocalize uniquely with 1) Sec23, a COPII vesicle marker that normally recycles back to the ER (Figure 8B; Lord *et al.*, 2013), and 2) TGN38, an integral membrane protein that normally cycles between the TGN and the cell surface (Figure 8F; Reaves *et al.*, 1993). This raises the intriguing possibility that uroplakins complexed with Sec23a and/or TGN38 are delivered via an unknown vesicular pathway from the TGN to the LDs. Finally, these results mean that it is unlikely that uroplakins are transferred directly from the ER exit

| Properties/markers[a] | | Figures | Normal mitochondria | Small intramitochondrial LDs (stage I labeled * in Figure 4, D–K) | Larger LDs in mitochondria with damaged or no cristae (stage II, **; Figure 4, L and M) or with cytoplasmic exposure (stage III, ***; Figure 5, A–F) | Autophagosome | Lysosome |
|---|---|---|---|---|---|---|---|
| **Size** | | **4, 5, 6, and 7, A–C** | **~0.5 μm** | **0.5–0.8 μm** | **1–5 μm** | **0.5–1.5 μm** | **1–2 μm** |
| Uroplakins | UPIa, II, IIIa, IIIb | 1, 6, 7, 8, 9, and 10 | – | ++ | ++ | + | + |
| Lipid | Lipophlic dyes | S1, F–H | – | ++ | ++ | | |
| PLIN1 and 2 | | 7, M and N | – | ++ | ++ | | |
| Mitochondrial markers | AIF, Cox4 | 7K and 7O | ++ | ++ | ++ | | |
| | Mitofusin | Unpublished data | + | ++ | ++ | | |
| | PINK1, PARK2 | 7L and unpublished data | – | + | ++ | | |
| | Mito-ID Green, MMP | 7, A–J | + | +++ | +++ | | |
| ER | Sec23A | 8B | – | ++ | ++ | | |
| | Calnexin | 8D | – | +/– | + | | |
| Golgi | GM130 | 8E | – | – | – | | |
| | TGN38 | 8F | – | + | ++ | | |
| Autophagosome | LC3 | 9, B–D | – | ++ | ++ | ++ | |
| Lysosome | LAMP1 | 1, J–L, and 9E | – | + | + | + | ++ |

[a]See text for the references of the markers.

**TABLE 1:** Progressive changes in the size and antigenic properties of mitochondrial lipid droplets during different stages of lipid drop (LD) formation in the Snx31-KO urothelial cells.

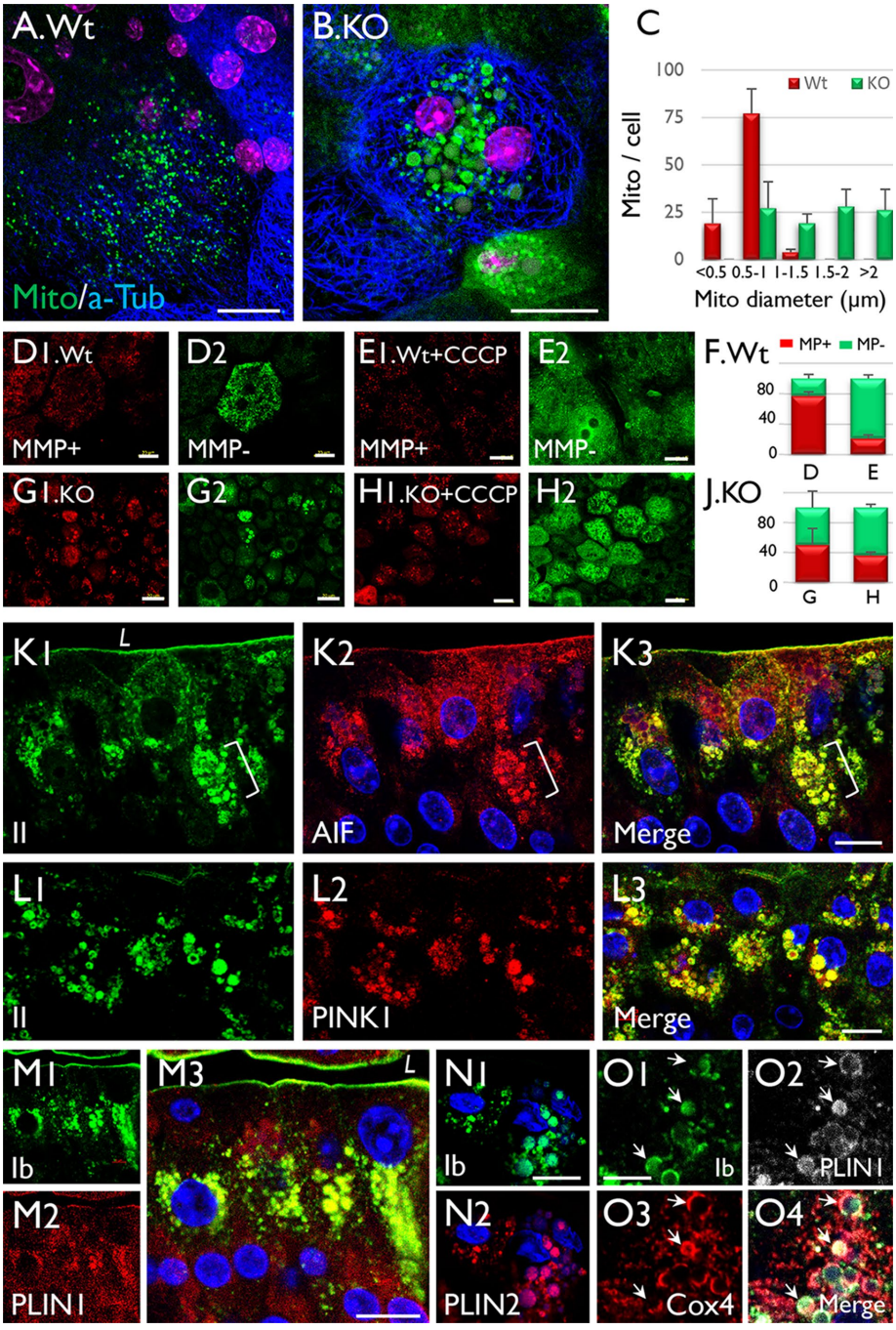


FIGURE 7: Mitochondrial enlargement is accompanied by the formation of uroplakin-positive lipid droplets in *Snx31*-KO urothelial cells. (A, B) Staining of (A) normal and (B) *Snx31*-KO urothelial (whole-mount) preparations using Mito-ID Green, a mitochondria dye. Note that while most of the mitochondria in (A) normal urothelial cells are <1 μm wide, those in (B) *Snx31*-KO are >1 μm (panel C). (D–J) Comparison of the mitochondrial membrane potential (MMP) in whole-mount preparations of (D, E) normal and (G, H) *Snx31*-KO mouse urothelia that were (D, G) untreated or (E, H) treated with CCCP (a mitochondrial oxidative phosphorylation uncoupler leading to decreased MMP). Mitochondria with high and low MMP are stained in red and green, respectively. SD based on the analysis of mitochondria from 20 cells. (K–O) Paraffin sections of mouse bladder urothelia from *Snx31*-KO mice were double stained using antibodies to uroplakins (green) and organelle markers in various combinations, as indicated: (K) uroplakin II and AIF, a mitochondrial marker; (L) UPII and PINK1, a mitophagy marker; (M) UPIb and Perilipin 1 (PLIN1), a LD marker; (N) UPIb and Perilipin 2 (PLIN2), another lipid droplet marker; and (O) UPIb, Cox4 (another mitochondrial marker), and PLIN1. Note in O the colocalization of uroplakins with mitochondrial and LD markers (arrows) in some droplets indicating the accumulation of uroplakin-containing LDs in mitochondria. Scale bars = 10 μm in K–L, N, and O; 20 μm in A and B, and D–H; 50 μm in M.

sites (Omari *et al.*, 2018), without going through the Golgi/TGN pathway, into the mitochondrial LDs.

### Mitochondrial LD formation versus ER stress, autophagy, and apoptosis

Although it has been suggested that there is significant cross-talk between the unfolded protein response, autophagy, and altered mitochondrial function (Senft and Ronai, 2015), it is unclear whether ER stress, which is a constant feature in all the KO urothelia and in the urothelia of the As-treated mice, plays a role in mitochondrial LD formation. It seems clear, however, that the extent of autophagy-mediated lysosomal degradation is correlated with the extent of giant LD formation, with *Snx31*-KO offering the most striking example of the latter (Figures 5–7). In contrast, in the *UP*-KOs (Figure 10) and the urothelium of the As-treated mice (Figure 11) where LDs are mostly intramitochondrial, autophagy/lysosomal degradation is less prevalent. This suggests that autophagy/lysosomal degradation occurs primarily when there is a large load of excessive/misassembled membrane proteins that needs to be sequestered and digested.

It is curious why the mitochondrial LD pathway has so far only been seen in the urothelium (and perhaps oocytes as well; Massover, 1971). A key feature of the mitochondrial LD pathway, as we reported here in the urothelium, is the continued expansion of LDs, resulting in mitochondrial damage (Figures 4, G–M, and 7, A–J) and destruction (Figures 4 and 5), which can lead to the release of proapoptotic proteins. Given the fact that almost all superficial cells in the *Snx31*-KO eventually form uroplakin-positive LDs (Figure 1L), it is remarkable that the urothelium survives at all, with only limited apoptosis being apparent (Figure 9, E and F). This raises the question of whether the urothelium, which normally has the lowest turnover rate among all stratified epithelia (Walker, 1960), is uniquely resistant to mitochondrial proapoptotic signals. This hypothesis may explain why the mitochondrial LD pathway, which could be suicidal in other cell types, can operate in the urothelial superficial cells.

### Concluding remarks

We showed here that Snx31 provides a striking example of a tissue-specific MVB protein that enables the urothelial umbrella cells to process a tissue-specific cargo, that is, uroplakin membrane plaques, for lysosomal degradation. Our results indicate that

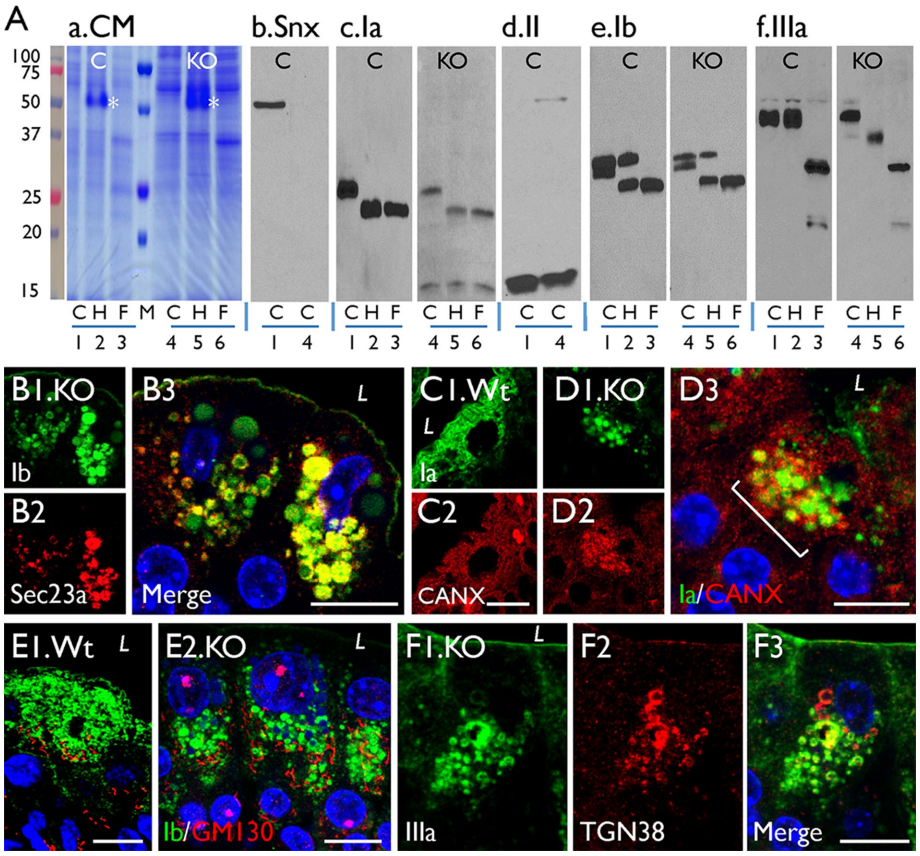


FIGURE 8: Uroplakins are processed through the ER-Golgi-TGN pathway in the *Snx31*-KO urothelia. (A) Assessing uroplakin trafficking through the ER-Golgi-TGN pathway based on their glycosylation and proteolytic processing status. Crude membrane proteins from the wild-type (lanes 1–3) and *Snx31*-KO (lanes 4–6) mouse urothelia were incubated with buffer (lanes 1 and 4; control or "C"), Endo H ("H," lanes 2 and 5; asterisks in panel a mark the added Endo H enzyme), or PNGase F (lanes 3 and 6; "F"). The electroblotted samples were stained with (a) Coomassie Blue (CM), or immunoblotted with antibodies to (b) Snx31, (c) UPIa, (d) UPII, (e) UPIb, or (f) UPIIIa. Note that, like in the wild-type urothelium, the glycans of UPIa of the *Snx31*-KO are Endo H sensitive, those of UPIb and IIIa are PNGase F sensitive, and that the 32 kDa pro-UPII is cleaved by the TGN-associated furin to yield the 15 kDa mature UPII. Five wild-type and 15 Snx31-KO mice were used for protein collection. (B) Double staining of KO urothelial sections for UPIb (green) and Sec23a, an ER marker. (C, D) Double staining of the Wt and *Snx31*-KO urothelial sections for uroplakin Ia (green) and ER stress markers calnexin (C2, D2). (E, F) Double staining of KO urothelial sections for UPIb (green) and (E) GM130, a Golgi marker, or (F) TGN38, a TGN marker. Scale bars = 10 μm in B–F.

MVBs play an active role in suppressing the endocytic degradation of the uroplakins (Figure 11P), and that the failure of this MVB regulation activates a mitochondrial LD pathway for the autophagy/lipophagy-mediated degradation of the excessive uroplakin membranes (Figure 11Q). The fact that this mitochondrial LD pathway is induced not only by Snx31-KO, but also by uroplakin imbalance and arsenite, a bladder carcinogen, suggests that it serves as a versatile detoxification mechanism not only to degrade the excessive/misassembled membranes, but also to protect the urothelium from arsenite (Figure 11Q). The discovery of this mitochondria-LD pathway offers new opportunities for expanding our understanding of mitochondrial biology, lipid droplet formation, and regulation of membrane degradation. Additional studies are needed to determine the mechanism of intramitochondrial LD formation, how the excessive/imbalanced membrane proteins are delivered to the interior of the LDs, the functional significance of As-induced mitochondrial LD formation, and whether this pathway also operates in some other cell types, such as oocytes, which also express uroplakins (Liao *et al.*, 2018). Additional studies are also needed to determine whether patients with certain mitochondrial defects may be more susceptible to arsenite-induced and other carcinogen-induced bladder toxicity and tumor formation, and whether the novel urothelial features uncovered here can be explored to mitigate certain bladder conditions involving malfunctioning urothelia, such as interstitial cystitis and overactive bladder.

## MATERIALS AND METHODS

### Animals

Unless indicated, all animals used were female, and between 8 and 12 wk of age. Conventional and conditional SNX31-, UPII-, UPIIIa-knockout, as well as C57BL/6TN Wt control mice were bred at New York University, and the arsenic (+3 oxidation state) methyltransferase knockout (*As3mt*-KO) mice were bred in S. M. Cohen's lab at the University of Nebraska. Mice were fed ad libitum consumption with drinking water containing 43.3 ppm sodium arsenite ($NaAs^{III}$; AsNaO2, anhydrous; Sigma, St. Louis, MO) for 28 d (Dodmane *et al.*, 2014). All animal protocols were consistent with guidelines set by the National Institutes of Health and approved by the Institutional Animal Care and Use Committees, New York University School of Medicine and University of Nebraska Medical Center.

### Reagents

The reagents used in this study and their sources are listed as follows: RNA Later, Applied BiosystemsHigh-Capacity cDNA Reverse Transcription Kit, DreamTaq Green PCR Master Mix, Supersignal West Pico chemiluminescent substrate (Thermo Fisher Scientific, New York, NY); RNeasy Plus Mini kit (Qiagen, Germantown, MD); nitrocellulose membrane (Bio-Rad, Hercules, CA); Endo H and PNGase F (New England BioLabs, Ipswich, MA); Fluorogel DABCO (Electron Microscopy Sciences, Hatfield, PA; Mito-ID Green detection kit and Mito-ID Membrane potential detection kit were purchased from Enzo Life Sciences (Farmingdale, NY). See Supplemental Table S1 for a list of antibodies and probes.

### Antibodies to uroplakins and Western blotting

Our antibodies to individual uroplakins (Ia, Ib, II, IIIa, and IIIb) are either mouse monoclonal or rabbit antisera against synthetic peptides (Wu *et al.*, 1994, 1995; Liang *et al.*, 2001; Liao *et al.*, 2018). They have been shown to be monospecific, that is, they recognize a single, correct antigen band when immunoblotting against total urothelial proteins (Figures 1D2 and 8A). For immunoblotting, 15 μg of total urothelial SDS extract was loaded into each lane of a 12.5% SDS–PAGE gel and separated by electrophoresis. A portion of the gel was removed for silver staining

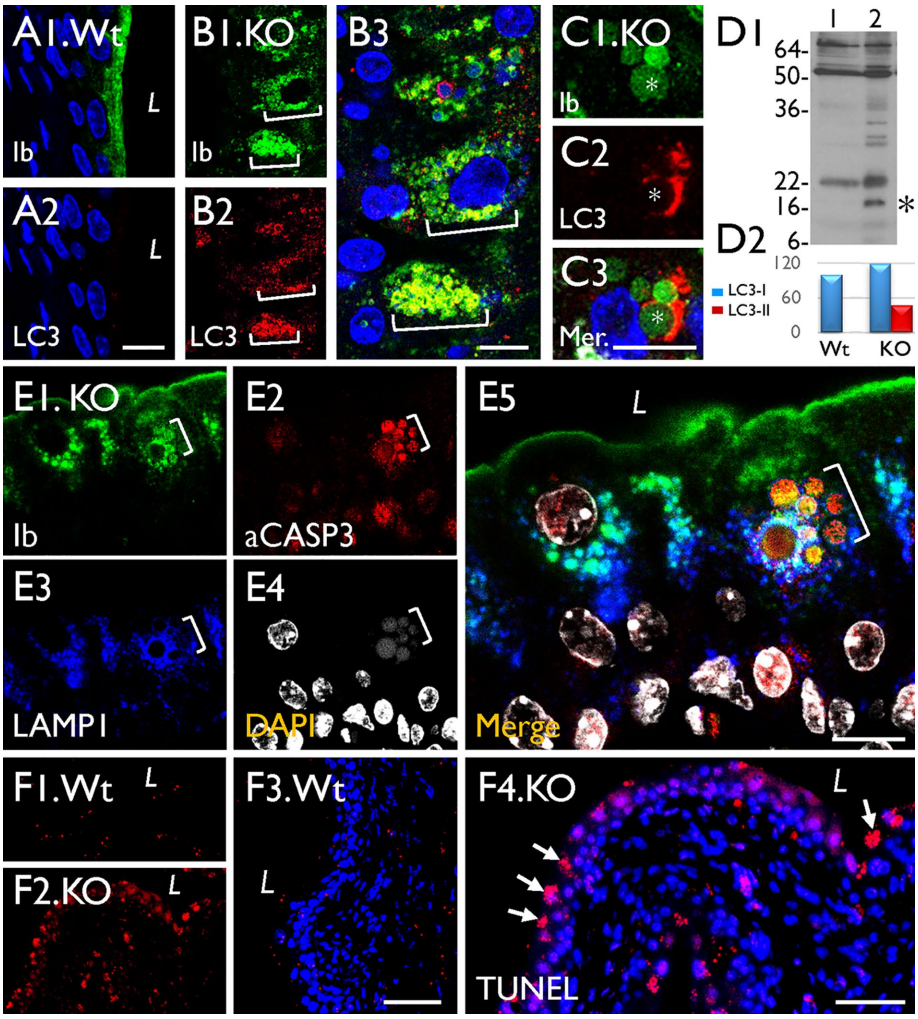


FIGURE 9: The UP-positive LDs in *Snx31*-KO urothelium are associated with autophagy markers. (A–C) Paraffin sections of urothelia from normal (Wt) or *Snx31*-KO mice (as marked) were double stained using antibodies to UPIb and LC3, an autophagy marker. (D) Immunoblotting showing the appearance in the KO urothelium of a 16-kDa band (*) indicating LC3 activation (lane 2 vs. control in lane 1). Four animals from each line were used. (E) Costaining of the KO urothelium for UPIb, caspase 3, LAMP1, and DAPI showing the partial colocalization of UP and LAMP1 and induction of apoptosis. (F) TUNEL assay for the Wt (F1, F3) or *Snx31*-KO urothelia (F2, F4). Note the colocalization of uroplakins with markers of autophagy (B3), and the expression of apoptotic markers in some of the LD-laden cells. Scale bars = 10 μm in all IF staining panels.

and the proteins in the remainder were transferred onto 0.2-μm-pore-sized nitrocellulose membrane. These membranes were first blocked in PBS-Tween containing 5% nonfat dry milk for 1 h at 25°C, and then incubated serially in primary and horseradish peroxidase (HRP)-conjugated secondary antibodies overnight at 4°C and for 2 h at 25°C, respectively (Wu *et al.*, 1994, 1995; Deng *et al.*, 2002). Visualization was performed using Supersignal West Pico chemiluminescent substrate.

### Immunofluorescence and microscopy

Bladders from Wt, SNX31 knockout, and UP-KO mice were fixed with 4% formaldehyde in phosphate-buffered saline (PBS), prepared into frozen or paraffin blocks, then sectioned (5 μm thick). The deparaffinized sections were subjected to antigen retrieval before incubation with PBS containing 5% bovine serum albumin and 1% donkey serum at 25°C, and then with primary antibodies in the same buffer at 4°C overnight, followed by a 1-h incubation with secondary antibodies. Samples were mounted using Fluorogel DABCO as an anti-fading mounting medium, and imaged using a Zeiss LM700 confocal microscope (Liang *et al.*, 2001; Liao *et al.*, 2018).

### Electron microscopy

TEM was performed as described earlier (Zhou *et al.*, 2012; Vieira *et al.*, 2014). Briefly, mouse bladders were cut into 1-mm cubes, fixed for 2 h at 25°C in a 2.5% glutaraldehyde and 2% paraformaldehyde (PFA)/0.1 M cacodylate buffer solution, and processed. In the case of immunoelectron microscopy, the fixative used was a combination of 2% PFA and 0.2% glutaraldehyde in 0.1M cacodylate buffer. Tissue sections were incubated with primary antibodies at 4°C overnight and then with gold-conjugated secondary antibodies. In both cases, sections were viewed using a CM12 TEM and photographed with a Gatan (4K × 2.7K) digital camera. TEM tomography was done by collecting serial images from 150-nm-thick sections by tilting the specimen every 2° from +70 to –70 using a CM200 TEM, and then processed to generate a video.

Serial block-face SEM samples were prepared according to the OTO (O-osmium, T-thiocarbohydrazide, O-osmium) method (Tapia *et al.*, 2012), and imaged with Zeiss GEMINI300 FESEM equipped with a Gatan 3View automatic microtome. The system was set to cut 90-nm slices, and images were recorded after each round of section from the block face using the SEM beam at 1.2 keV with a dwell time of 2.0 μs/pixel with pixel size at 3 nm. Data acquisition occurred in an automated way using the Auto Slice and View G3 software. A stack of 36 slices was aligned, assembled using ImageJ. Segmentation and video were generated by ORS Dragonfly 3.6 software.

### Whole-mount preparation of mouse urothelium for the live staining of mitochondria

Mouse bladder was bisected sagittally, stretched gently, pinned onto a paraffin wax plate in the bottom of a 60-mm Petri dish, and fixed in 4% formaldehyde in PBS at 25°C for 1 h, unpinned and washed three times with PBS at 25°C. The urothelium with a thin layer of submucosa was physically peeled off from the bladder wall using a pair of forceps, permeabilized with 1% Triton X-100 in PBS at 25°C for 1 h in a 24-well dish, and washed with PBS (Wankel *et al.*, 2016). For mitochondrial staining, the tissue was incubated with a mixture of Mito-ID Green dye and anti-tubulin at 37°C for 2 h, washed with PBS, and incubated with a secondary antibody at 25°C for 1 h and then DAPI (4′, 6-diamidino-2-phenylindole) for 5 min. The flattened whole mount with the urothelium facing up was mounted with Fluorogel DABCO as an anti-fading mounting medium, and visualized with a Zeiss LM700 confocal microscope. For the assessment of MMP, the

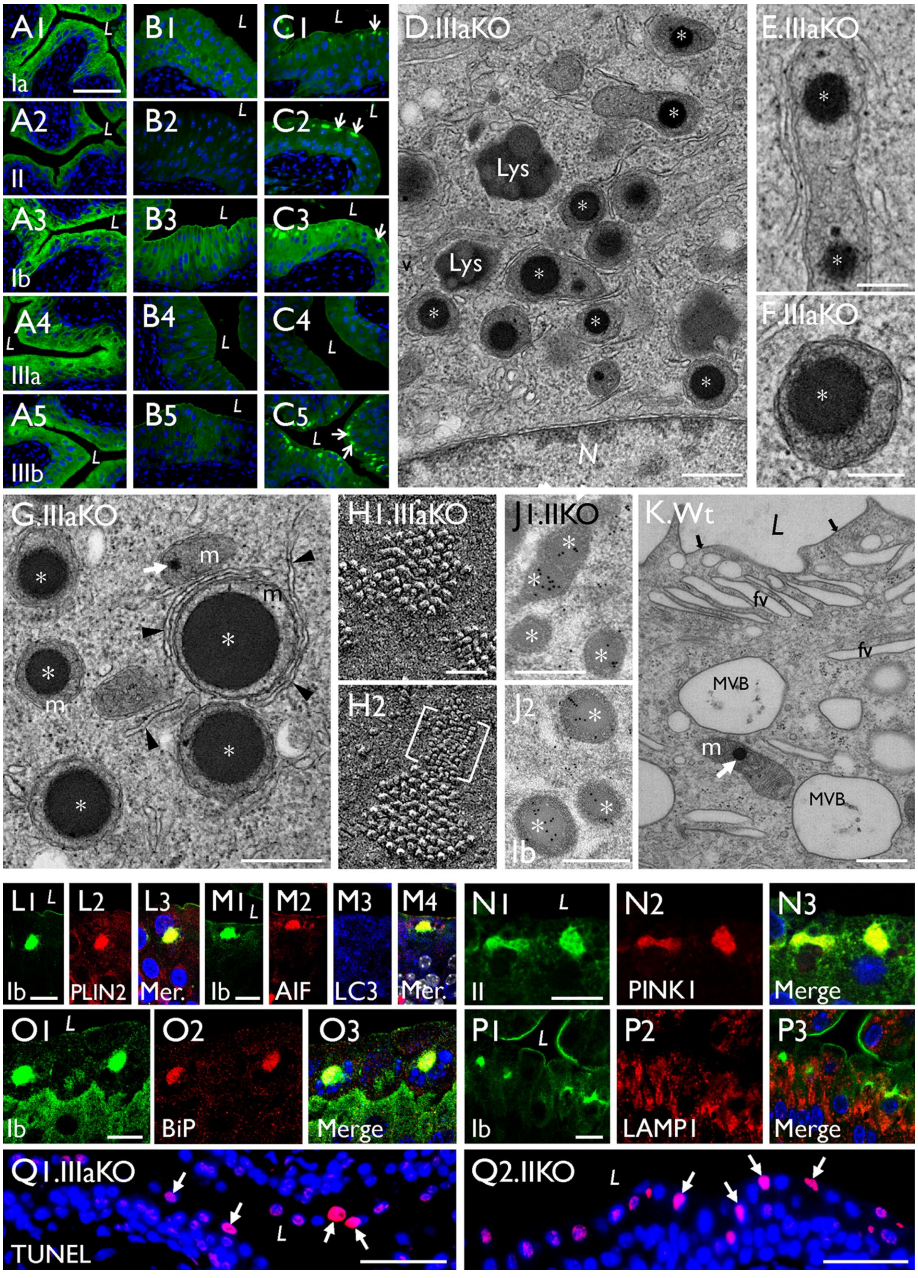


**FIGURE 10:** Mitochondrial LDs are also present in uroplakin-KO urothelia. (A–C) Paraffin sections of (A) control, (B) *UPII*-KO, and (C) *UPIIIa*-KO mouse urothelia were stained using antibodies to UPIa, II, Ib, IIIa, and IIIb as indicated; note in C that UPIIIa-KO leads to the formation of cytoplasmic aggregates containing all the remaining uroplakin types (arrows). (D–G) TEM of *UPIIIa*-KO urothelial superficial cells showing the perinuclear accumulation of LD-containing mitochondria (stages I and II; * and **, respectively); some appear to be interacting with isolation membranes (arrowheads). (H1, H2) The quick-freeze deep-etch (QFDE) images of the apical surface of a *UPIIIa*-KO superficial cell (the E face) showing small patches of hexagonally packed 16-nm uroplakin particles, as well as a patch of abnormal 3–4-nm particles containing UPIa/II-Ib/IIIb (bracketed). (J1, J2) Immunogold EM of a *UPII*-KO superficial cell showing the UP-positive intramitochondrial LDs (*). (K) An occasional wild-type umbrella cell showing a mitochondrion containing a small intramitochondrial LD (white arrow). (L–Q) Paraffin sections of the *UPIIIa*-KO urothelium were double stained using antibodies to uroplakins and (L) PLIN2, (M) AIF and LC3, (N) PINK1, (O) N-BiP (ER stress), and (P) LAMP1. "Mer" denotes a merged image. (Q1, Q2) TUNEL assay for paraffin sections of (Q1) *UPIIIa*-KO and (Q2) *UPII*-KO urothelium. Note the colocalization of these UP-KO–related intramitochondrial LDs with markers of (L) lipid droplet, (M) mitochondria, (N) mitophagy, and (O) ER stress marker, but not with (M) markers for autophagy or (P) lysosome. Scale bars = 50 nm in H; 0.2 μm in E and F; 0.5 μm in D, G, J, and K; 10 μm in L–P; 50 μm in A–C and Q.

nonfixed, whole-mount bladder was incubated with the Mito-ID Membrane potential detection reagent according to the manufacturer's manual (Enzo Life Sciences, Farmingdale, NY) at RT for 15 min, then with Hoechst 33258 for 5 min and visualized with a Zeiss confocal microscopy.

### Deglycosylation

Insoluble urothelial proteins from Wt and SNX31 knockout mouse bladders were dissolved in 0.5% SDS and 40 mM dithiothreitol, and incubated at 30°C for 6 h with endoglycosidase H (200 U/100 μg protein) in 50 mM sodium citrate buffer, pH 5.5; or with *N*-glycosidase F (200 U/100 μg protein) in 50 mM sodium phosphate buffer, pH 7.5, plus 1% NP40. Protease inhibitors were included in all the buffers. Samples were resolved by 15% SDS–PAGE and then stained with Coomassie blue or transferred onto nitrocellulose membrane to react with anti-uroplakin antibodies (Wu and Sun, 1993; Liang *et al.*, 1999).

### RT-PCR

RNA was first stabilized using RNA Later, before being extracted using a Qiagen RNeasy kit. cDNA synthesis was performed with Applied Biosystems' High Capacity cDNA Reverse Transcription kit, and amplified using DreamTaq Green PCR Master Mix. The resultant products were separated in a 1.5% agarose gel, and visualized under UV illumination. All procedures were carried out according to the protocols provided by the respective manufacturers of the above products.

### Phylogenetic analysis of Snx31 and uroplakins

Uroplakin, SNX31, and SNX17 sequences were retrieved from the ENSEMBLE (http://www.ensembl.org/index.html) server and/or the National Center for Biotechnology Information (NCBI; www.ncbi.nlm.nih.gov/) using known sequences as bytes and the NCBI BLAST programs; some sequences were corrected using ESTs (expressed sequence tags) from EST databases. Phylogenetic analyses of these sequences were conducted as reported previously (Desalle *et al.*, 2014).

### Congruence analysis

The coevolutionary interaction of Snx31 with UPs was examined using the same approach as we reported earlier (Garcia-Espana *et al.*, 2006), except we have broadened the phylogenetic scope of species and performed more evolutionary

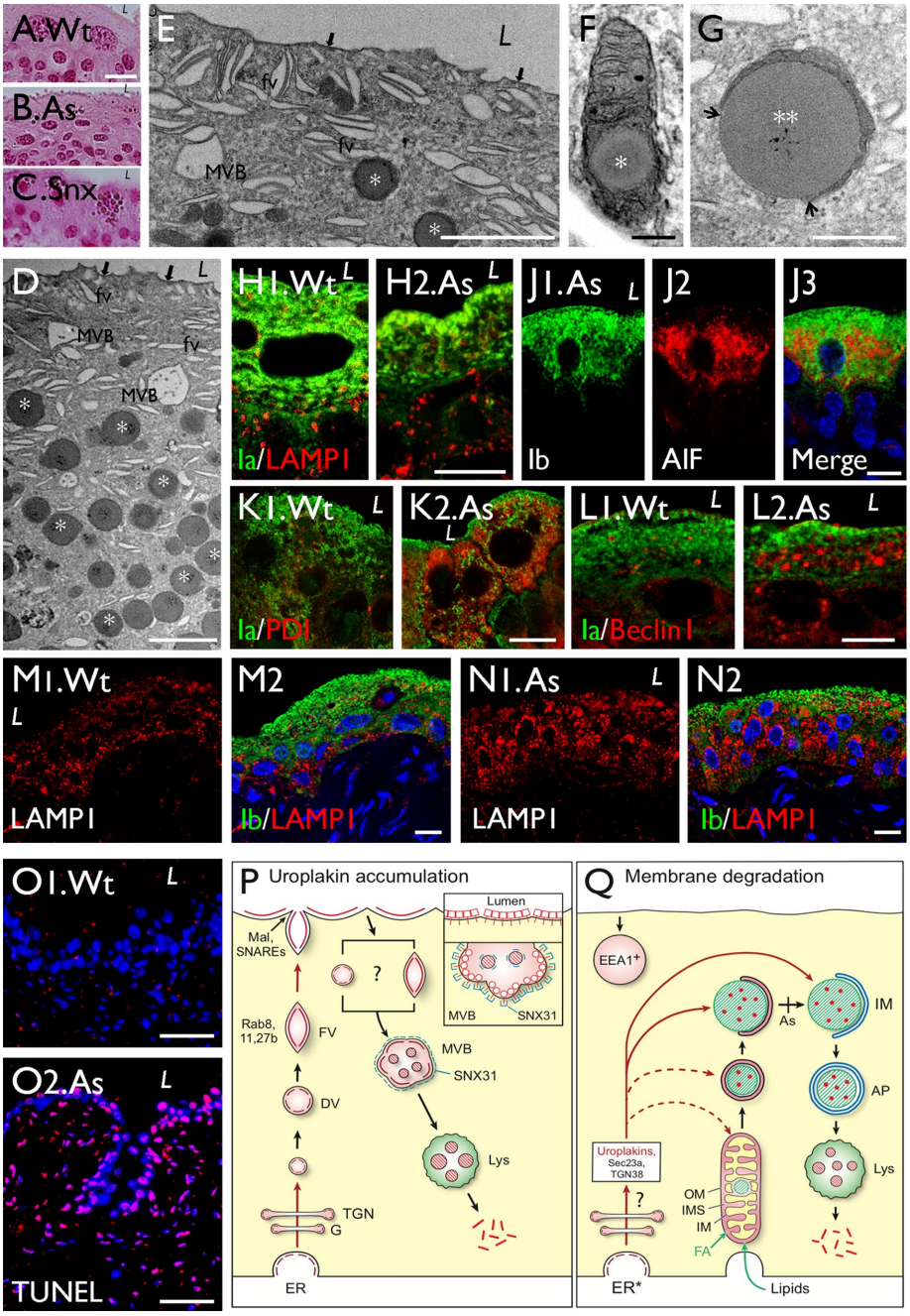


**FIGURE 11:** Urothelial mitochondrial LDs are also induced by arsenite treatment; models illustrating Snx31 function and mitochondrial LD-mediated uroplakin degradation. Paraffin sections of urothelia of (A) a wild-type mouse, (B) a sodium arsenite (As)-treated *Asmt3*-KO mouse, and (C) a *Snx31*-KO mouse, were stained with eosin. Note similarly stained granules in As-treated urothelium and *Snx31*-KO samples. (D–G) Transmission EM of the urothelium from the As-treated *Asmt3*-KO mouse. Note in D and E the accumulation of mitochondrial LDs similar to the LDs in the *Snx31*-KO mice (cf. Figure 2B), and the intact apical urothelial plaques (black arrows), fusiform vesicles (FVs) and multivesicular bodies (MVBs). (H–O) Double immunofluorescence staining of urothelial section from control (Wt) or As-treated (marked "As") mice using antibodies to uroplakin plus (H) LAMP1 (late endosome/lysosome), (J) AIF (mitochondria), (K) PDI (ER stress), (L) Beclin I (autophagy), and (M, N) LAMP1. (O) TUNEL assay. Note in H2 and N2 that the urothelium from the As-treated mouse has normal, relatively uniform cytoplasmic distribution of uroplakin vesicles. (P, Q) Models illustrating the uroplakin trafficking patterns in (P) normal and (Q) *Snx31*-KO urothelial superficial cells. (P) In normal umbrella cells, uroplakins go through the ER/Golgi/TGN pathway and are delivered to discoidal and fusiform vesicles that undergo Rab8/11/27b-mediated apical targeting, and Mal-facilitated and Snare-mediated apical membrane fusion (Zhou *et al.*, 2012; Wankel *et al.*, 2016). Apical plaques are endocytosed via small uroplakin-positive vesicles or "dilated fusiform vesicles," which are incorporated into plaque-lined multivesicular bodies. The inset depicts the binding of Snx31 to the cytoplasmic tail of the MVB-associated UPIIIa inducing a global conformational change of the uroplakin plaques, allowing them to adopt a higher degree of curvature than that of apical plaques in order to stabilize the MVB structure, and to facilitate the formation of intraluminal vesicles (ILVs). (Q) Snx31 deficiency induces the formation of intramitochondrial LDs, which receive the uroplakin/Sec23a/TGN38 complex and undergo autophagy-mediated lysosomal degradation. Similar mitochondrial pathologies are present in *UP*-KO and As-treated urothelium, although in these cases the LDs rarely become denuded (the approximate "blockage" point is indicated by a vertical bar marked "As"). The fact that LD formation can occur in As-treated urothelium without uroplakin degradation suggests that the former represents a general detoxification mechanism that can remove not only excessive or abnormally assembled uroplakins, but also cytotoxic metals. The EEA1+ vacuoles (Figure S1J) are presumably early endosomes that have little to do with uroplakin trafficking. Abbreviations: AP (autophagosome), As (arsenite), DV (discoidal vesicle), EEA1 (early endosome antigen 1), FV (fusiform vesicle), IM (isolation membrane), Lys (lysosome), IMS (mitochondrial intermembrane space), OM (mitochondrial outer membrane), and MVB (multivesicular body). See text for details. Scale bars = 0.2 µm in F, 0.5 µm in G, 2 µm in D and E, 10 µm in A–C and H–N, and 50 µm in O.

congruence tests including the Shimodaira-Hasegawa (SH) test (purple line in Figure 1C2; Shimodaira and Hasegawa, 1999; Shimodaira, 2002), mirrortree method (MT) (green; Ochoa and Pazos, 2010), and incongruence length difference (ILD) (red; Farris *et al.*, 1994). The MT program is based on distance comparisons and SH and ILD are based on character. The comparisons measure the similarity of tree topology of the gene trees for the two genes in a comparison. Snx17, which is not known to interact with uroplakins, was used as a negative control, with no congruence detected with any of the UPs (unpublished data).


## ACKNOWLEDGMENTS

We acknowledge the excellent services provided by the New York University School of Medicine Core Laboratories on Microscopy, Experimental Pathology, and Rodent Genetic Engineering (supported in part by National Institutes of Health [NIH] Grant no. NCRR RR-023704, Grant no. RR-024708, and Grant no. S10 OD-019974). This work was supported in part by the NIH (Grant

no. DK-52206 for T.-T.S., X.R.W., and M.J.R.; and DK-39753 for T.-T.S.), and the Spanish Ministerium de Economic y Competitive FIS PI16/00504 (A.G.-E.). X.R.W. is a Department of Veterans Affairs Biomedical Laboratory Research and Development (VA BLR&D) Research Career Scientist (1IK6BX004479). We dedicate this article to Herbert Lepor, Chairman of New York University Urology, for his unwavering support of our work on urothelial biology for the past 25 years.

## REFERENCES

Amano O, Kataoka S, Yamamoto TY (1991). Turnover of asymmetric unit membranes in the transitional epithelial superficial cells of the rat urinary bladder. Anat Rec 229, 9–15.

American Cancer Society (2019). Key Statistics for Bladder Cancer (American Cancer Society). www.cancer.org/cancer/bladder-cancer/about/key-statistics.html.

Cohen S (2018). Lipid droplets as oganelles. Int Rev Cell Mol Biol 337, 83–110.

Deng FM, Liang FX, Tu L, Resing KA, Hu P, Supino M, Hu CC, Zhou G, Ding M, Kreibich G, *et al*. (2002). Uroplakin IIIb, a urothelial differentiation marker, dimerizes with uroplakin Ib as an early step of urothelial plaque assembly. J Cell Biol 159, 685–694.

Desalle R, Chicote JU, Sun TT, Garcia-Espana A (2014). Generation of divergent uroplakin tetraspanins and their partners during vertebrate evolution: identification of novel uroplakins. BMC Evol Biol 14, 13.

Dodmane PR, Arnold LL, Muirhead DE, Suzuki S, Yokohira M, Pennington KL, Dave BJ, Lu X, Le XC, Cohen SM (2014). Characterization of intracellular inclusions in the urothelium of mice exposed to inorganic arsenic. Toxicol Sci 137, 36–46.

Durcan TM, Fon EA (2015). The three "P"s of mitophagy: PARKIN, PINK1, and post-translational modifications. Genes Dev 29, 989–999.

Eskelinen EL (2006). Roles of LAMP-1 and LAMP-2 in lysosome biogenesis and autophagy. Mol Aspects Med 27, 495–502.

Farris JS, Källersjö M, Kluge AG, Bult C (1994). Testing significance of incongruence. Cladistics 10, 315–319.

Flores-Mireles AL, Walker JN, Caparon M, Hultgren SJ (2015). Urinary tract infections: epidemiology, mechanisms of infection and treatment options. Nat Rev Microbiol 13, 269–284.

Fromme JC, Orci L, Schekman R (2008). Coordination of COPII vesicle trafficking by Sec23. Trends Cell Biol 18, 330–336.

Garcia-España A, Chung PJ, Zhao X, Lee A, Pellicer A, Yu J, Sun TT, Desalle R (2006). Origin of the tetraspanin uroplakins and their co-evolution with associated proteins: implications for uroplakin structure and function. Mol Phylogenet Evol 41, 355–367.

Glabe CG (2006). Common mechanisms of amyloid oligomer pathogenesis in degenerative disease. Neurobiol Aging 27, 570–575.

Hanson PI, Cashikar A (2012). Multivesicular body morphogenesis. Annu Rev Cell Dev Biol 28, 337–362.

Hansson Petersen CA, Alikhani N, Behbahani H, Wiehager B, Pavlov PF, Alafuzoff I, Leinonen V, Ito A, Winblad B, Glaser E, *et al*. (2008). The amyloid β-peptide is imported into mitochondria via the TOM import machinery and localized to mitochondrial cristae. Proc Natl Acad Sci USA 105, 13145–13150.

Hu P, Deng FM, Liang FX, Hu CM, Auerbach AB, Shapiro E, Wu XR, Kachar B, Sun TT (2000). Ablation of uroplakin III gene results in small urothelial plaques, urothelial leakage, and vesicoureteral reflux. J Cell Biol 151, 961–972.

Hu CC, Liang FX, Zhou G, Tu L, Tang CH, Zhou J, Kreibich G, Sun TT (2005). Assembly of urothelial plaques: tetraspanin function in membrane protein trafficking. Mol Biol Cell 16, 3937–3950.

Hu P, Meyers S, Liang FX, Deng FM, Kachar B, Zeidel ML, Sun TT (2002). Role of membrane proteins in permeability barrier function: uroplakin ablation elevates urothelial permeability. Am J Physiol Renal Physiol 283, F1200–F1207.

Kachar B, Liang F, Lins U, Ding M, Wu XR, Stoffler D, Aebi U, Sun T-T (1999). Three-dimensional analysis of the 16 nm urothelial plaque particle: luminal surface exposure, preferential head-to-head interaction, and hinge formation. J Mol Biol 285, 595–608.

Khandelwal P, Abraham SN, Apodaca G (2009). Cell biology and physiology of the uroepithelium. Am J Physiol Renal Physiol 297, F1477–F1501.

Kong XT, Deng FM, Hu P, Liang FX, Zhou G, Auerbach AB, Genieser N, Nelson PK, Robbins ES, Shapiro E, *et al*. (2004). Roles of uroplakins in plaque formation, umbrella cell enlargement, and urinary tract diseases. J Cell Biol 167, 1195–1204.

Kyrylkova K, Kyryachenko S, Leid M, Kioussi C (2012). Detection of apoptosis by TUNEL assay. Methods Mol Biol 887, 41–47.

Larsen BD, Sorensen CS (2017). The caspase-activated DNase: apoptosis and beyond. FEBS J 284, 1160–1170.

Lashuel HA (2005). Membrane permeabilization: a common mechanism in protein-misfolding diseases. Sci Aging Knowledge Environ 2005, pe28.

Liang F, Kachar B, Ding M, Zhai Z, Wu XR, Sun T-T. (1999). Urothelial hinge as a highly specialized membrane: detergent-insolubility, urohingin association, and in vitro formation. Differentiation 65, 59–69.

Liang FX, Riedel I, Deng FM, Zhou G, Xu C, Wu XR, Kong XP, Moll R, Sun TT (2001). Organization of uroplakin subunits: transmembrane topology, pair formation and plaque composition. Biochem J 355, 13–18.

Liao Y, Chang HC, Liang FX, Chung PJ, Wei Y, Nguyen TP, Zhou G, Talebian S, Krey LC, Deng FM, *et al*. (2018). Uroplakins play conserved roles in egg fertilization and acquired additional urothelial functions during mammalian divergence. Mol Biol Cell 29, 3128–3143.

Lin MT, Beal MF (2006). Mitochondrial dysfunction and oxidative stress in neurodegenerative diseases. Nature 443, 787–795.

Liu W, Duan X, Fang X, Shang W, Tong C (2018). Mitochondrial protein import regulates cytosolic protein homeostasis and neuronal integrity. Autophagy 14, 1293–1309.

Liu Y, Memet S, Saban R, Kong X, Aprikian P, Sokurenko E, Sun TT, Wu XR (2015). Dual ligand/receptor interactions activate urothelial defenses against uropathogenic *E. coli*. Sci Rep 5, 16234.

Lord C, Ferro-Novick S, Miller EA (2013). The highly conserved COPII coat complex sorts cargo from the endoplasmic reticulum and targets it to the golgi. Cold Spring Harb Perspect Biol 5, a013367.

Lotan Y, Kamat AM, Porter MP, Robinson VL, Shore N, Jewett M, Schelhammer PF, deVere White R, Quale D, Lee CT, *et al*. (2009). Key concerns about the current state of bladder cancer: a position paper from the Bladder Cancer Think Tank, the Bladder Cancer Advocacy Network, and the Society of Urologic Oncology. Cancer 115, 4096–4103.

Massover WH (1971). Intramitochondrial yolk-crystals of frog oocytes. II. Expulsion of intramitochondrial yolk-crystals to form single-membrane bound hexagonal crystalloids. J Ultrastruct Res 36, 603–620.

Min G, Wang H, Sun TT, Kong XP (2006). Structural basis for tetraspanin functions as revealed by the cryo-EM structure of uroplakin complexes at 6-A resolution. J Cell Biol 173, 975–983.

Mu FT, Callaghan JM, Steele-Mortimer O, Stenmark H, Parton RG, Campbell PL, McCluskey J, Yeo JP, Tock EP, Toh BH (1995). EEA1, an early endosome-associated protein. EEA1 is a conserved α-helical peripheral membrane protein flanked by cysteine "fingers" and contains a calmodulin-binding IQ motif. J Biol Chem 270, 13503–13511.

Negrete HO, Lavelle JP, Berg J, Lewis SA, Zeidel ML (1996). Permeability properties of the intact mammalian bladder epithelium. Am J Physiol 271, F886–F894.

Nillegoda NB, Wentink AS, Bukau B (2018). Protein disaggregation in multicellular organisms. Trends Biochem Sci 43, 285–300.

Ochoa D, Pazos F (2010). Studying the co-evolution of protein families with the Mirrortree web server. Bioinformatics 26, 1370–1371.

Olzmann JA, Carvalho P (2019). Dynamics and functions of lipid droplets. Nat Rev Mol Cell Biol 20, 137–155.

Omari S, Makareeva E, Roberts-Pilgrim A, Mirigian L, Jarnik M, Ott C, Lippincott-Schwartz J, Leikin S (2018). Noncanonical autophagy at ER exit sites regulates procollagen turnover. Proc Natl Acad Sci USA 115, E10099–E10108.

Ostrander DB, Zhang M, Mileykovskaya E, Rho M, Dowhan W (2001). Lack of mitochondrial anionic phospholipids causes an inhibition of translation of protein components of the electron transport chain. A yeast genetic model system for the study of anionic phospholipid function in mitochondria. J Biol Chem 276, 25262–25272.

Piper RC, Katzmann DJ (2007). Biogenesis and function of multivesicular bodies. Annu Rev Cell Dev Biol 23, 519–547.

Pol A, Gross SP, Parton RG (2014). Review: biogenesis of the multifunctional lipid droplet: lipids, proteins, and sites. J Cell Biol 204, 635–646.

Reaves B, Horn M, Banting G (1993). TGN38/41 recycles between the cell surface and the TGN: brefeldin A affects its rate of return to the TGN. Mol Biol Cell 4, 93–105.

Robenek H, Buers I, Robenek MJ, Hofnagel O, Ruebel A, Troyer D, Severs NJ (2011). Topography of lipid droplet-associated proteins: insights from freeze-fracture replica immunogold labeling. J Lipids 2011, 409371.

Ruan L, Zhou C, Jin E, Kucharavy A, Zhang Y, Wen Z, Florens L, Li R (2017). Cytosolic proteostasis through importing of misfolded proteins into mitochondria. Nature 543, 443–446.
Schapira AH (2012). Mitochondrial diseases. Lancet 379, 1825–1834.
Senft D, Ronai ZA (2015). UPR, autophagy, and mitochondria crosstalk underlies the ER stress response. Trends Biochem Sci 40, 141–148.
Shimodaira H (2002). An approximately unbiased test of phylogenetic tree selection. Syst Biol 51, 492–508.
Shimodaira H, Hasegawa M (1999). Multiple comparisons of log-likelihoods with applications to phylogenetic inference. Mol Biol Evol 16, 1114–1116.
Soreng K, Neufeld TP, Simonsen A (2018). Membrane trafficking in autophagy. Int Rev Cell Mol Biol 336, 1–92.
Sun T-T (2006). Altered phenotype of cultured urothelial and other stratified epithelial cells: implications for wound healing. Am J Physiol (Renal Physiol) 291, F9–F21.
Suzuki S, Arnold LL, Muirhead D, Lu X, Le XC, Bjork JA, Wallace KB, Ohnishi T, Kakiuchi-Kiyota S, Pennington KL, *et al*. (2008). Inorganic arsenic-induced intramitochondrial granules in mouse urothelium. Toxicol Pathol 36, 999–1005.
Tapia JC, Kasthuri N, Hayworth KJ, Schalek R, Lichtman JW, Smith SJ, Buchanan J (2012). High-contrast en bloc staining of neuronal tissue for field emission scanning electron microscopy. Nat Protoc 7, 193–206.
Thumbikat P, Berry RE, Zhou G, Billips BK, Yaggie RE, Zaichuk T, Sun TT, Schaeffer AJ, Klumpp DJ (2009). Bacteria-induced uroplakin signaling mediates bladder response to infection. PLoS Pathog 5, e1000415.
Tipping KW, van Oosten-Hawle P, Hewitt EW, Radford SE (2015). Amyloid fibres: inert end-stage aggregates or key players in disease? Trends Biochem Sci 40, 719–727.
Tu L, Sun TT, Kreibich G (2002). Specific heterodimer formation is a prerequisite for uroplakins to exit from the endoplasmic reticulum. Mol Biol Cell 13, 4221–4230.
Vieira N, Deng FM, Liang FX, Liao Y, Chang J, Zhou G, Zheng W, Simon JP, Ding M, Wu XR, *et al*. (2014). SNX31: a novel sorting nexin associated with the uroplakin-degrading multivesicular bodies in terminally differentiated urothelial cells. PLoS One 9, e99644.
Vincent AE, Ng YS, White K, Davey T, Mannella C, Falkous G, Feeney C, Schaefer AM, McFarland R, Gorman GS, *et al*. (2016). The spectrum of mitochondrial ultrastructural defects in mitochondrial myopathy. Sci Rep 6, 30610.
Walker BE (1960). Renewal of cell populations in the female mouse. Am J Anat 107, 95–106.
Wang CW (2016). Lipid droplets, lipophagy, and beyond. Biochim Biophys Acta 1861, 793–805.
Wang D, Liang J, Zhang Y, Gui B, Wang F, Yi X, Sun L, Yao Z, Shang Y (2012). Steroid receptor coactivator-interacting protein (SIP) inhibits caspase-independent apoptosis by preventing apoptosis-inducing factor (AIF) from being released from mitochondria. J Biol Chem 287, 12612–12621.
Wang H, Min G, Glockshuber R, Sun TT, Kong XP (2009). Uropathogenic *E. coli* adhesin-induced host cell receptor conformational changes: implications in transmembrane signaling transduction. J Mol Biol 392, 352–361.
Wankel B, Ouyang J, Guo X, Hadjiolova K, Miller J, Liao Y, Tham DK, Romih R, Andrade LR, Gumper I, *et al*. (2016). Sequential and compartmentalized action of Rabs, SNAREs, and MAL in the apical delivery of fusiform vesicles in urothelial umbrella cells. Mol Biol Cell 27, 1621–1634.
Wiedemann N, Pfanner N (2017). Mitochondrial machineries for protein import and assembly. Annu Rev Biochem 86, 685–714.
Wilfling F, Haas JT, Walther TC, Farese RV Jr (2014). Lipid droplet biogenesis. Curr Opin Cell Biol 29, 39–45.
Wu XR, Kong XP, Pellicer A, Kreibich G, Sun TT (2009). Uroplakins in urothelial biology, function, and disease. Kidney Int 75, 1153–1165.
Wu XR, Lin JH, Walz T, Haner M, Yu J, Aebi U, Sun T-T. (1994). Mammalian uroplakins. A group of highly conserved urothelial differentiation-related membrane proteins. J Biol Chem 269, 13716–13724.
Wu XR, Manabe M, Yu J, Sun T-T (1990). Large scale purification and immunolocalization of bovine uroplakins I, II, and III. Molecular markers of urothelial differentiation. J Biol Chem 265, 19170–19179.
Wu XR, Medina JJ, Sun T-T (1995). Selective interactions of UPIa and UPIb, two members of the transmembrane 4 superfamily, with distinct single transmembrane-domained proteins in differentiated urothelial cells. J Biol Chem 270, 29752–29759.
Wu XR, Sun T-T (1993). Molecular cloning of a 47 kDa tissue-specific and differentiation-dependent urothelial cell surface glycoprotein. J Cell Sci 106, 31–43.
Yu J, Lin JH, Wu XR, Sun T-T. (1994). Uroplakins Ia and Ib, two major differentiation products of bladder epithelium, belong to a family of four transmembrane domain (4TM) proteins. J Cell Biol 125, 171–182.
Zhou G, Liang FX, Romih R, Wang Z, Liao Y, Ghiso J, Luque-Garcia JL, Neubert TA, Kreibich G, Alonso MA, *et al*. (2012). MAL facilitates the incorporation of exocytic uroplakin-delivering vesicles into the apical membrane of urothelial umbrella cells. Mol Biol Cell 23, 1354–1366.
Zhou G, Mo WJ, Sebbel P, Min G, Neubert TA, Glockshuber R, Wu XR, Sun TT, Kong XP (2001). Uroplakin Ia is the urothelial receptor for uropathogenic *Escherichia coli*: evidence from in vitro FimH binding. J Cell Sci 114, 4095–4103.